Supplementary Materials for

Thermal catalytic reforming for hydrogen production with zero CO_2 emission

Mi Peng, Yuzhen Ge, Rui Gao, Jie Yang, Aowen Li, Zhiheng Xie, Qiaolin Yu, Jie Zhang, Asakura Hiroyuki, Hui Zhang, Zhi Liu, Qi Zhang, Jin Deng, Jihan Zhou, Wu Zhou, Graham J. Hutchings, Ding Ma

Corresponding author: dma@pku.edu.cn, wuzhou@ucas.ac.cn, jhzhou@pku.edu.cn, Hutch@Cardiff.ac.uk

The PDF file includes:

Other Supplementary Materials for this manuscript include the following:

Materials and Methods

Preparation of catalysts

The synthesis of α-MoC involved a two-step temperature-programmed process developed by our research group, utilizing self-made MoO_3 as a precursor (*1*, *2*). And α-MoC supported Pt/Ir catalysts were prepared by an incipient wetness impregnation (IWI) method.

Synthesis of MoO_3. Ammonium molybdate tetrahydrate ($(NH_4)_6Mo_7O_{24}\cdot 4H_2O$, Sinopharm Chemical Reagent) (10 g) was placed in a muffle oven, and the temperature was increased to 773 K at a rate of 10 K/min in air. The sample was held at 773 K for 4 hours and then allowed to cool naturally to room temperature. The resulting greyish-green powder was collected as self-prepared MoO_3 for subsequent use.

Synthesis of α-MoC. In a typical procedure, 800 mg of MoO_3 was loaded into a quartz tube and placed in a vertical furnace. The powder was heated from room temperature to 973 K in an ammonia atmosphere (160 ml min^{-1}; pre-purified gas) at a rate of 5 K/min and held at 973 K for 2 hours. After natural cooling to room temperature, the atmosphere was switched to a methane/hydrogen mixture (125 ml min^{-1}; $V_{(CH4)} : V_{(H2)} = 1 : 4$). The powder was then heated from room temperature to 973 K at a rate of 5 K min^{-1} and held at 973 K for another 2 h. The sample was then naturally cooled down to room temperature and passivated in 0.5% O_2 in Ar (30 ml/min) overnight.

Synthesis of α-MoC supported Pt/Ir catalysts. 100 mg of passivated α-MoC was dispersed in 10 mL of deionized water, and appropriate amounts of $H_2PtCl_6\cdot 6H_2O$ and/or $IrCl_3$ aqueous solution was added dropwise to obtain the desired loadings of Pt and/or Ir. The slurry was stirred for 2 hours at room temperatures and dried using rotary evaporator. Catalyst with the Pt/Ir weight loading of x% was named as xPt/α-MoC or xIr/α-MoC. Before each catalytic evaluation, the catalyst was *in-situ* activated in the fix-bed reactor.

SiO_2 supported PtIr catalyst. SiO_2 supported PtIr catalyst was prepared using the same incipient wetness impregnation (IWI) method. Before catalytic evaluation, the catalyst was pre-reduced with 10% H_2 in Ar (30 ml min^{-1}) at 573K for 2 hours.

NDG supported Pt catalyst. NDG supported Pt catalyst was prepared by incipient wetness impregnation method (*3*). Before catalytic evaluation, the catalyst was pre-reduced with 10% H_2 in Ar (30 ml min^{-1}) at 473K for 2 hours.

Catalytic performance evaluation

The catalytic performance evaluation was conducted in a continuous flow fixed-bed quartz reactor at atmospheric pressure. The 100 mg catalyst (40-60 mesh) was diluted with 800 mg quartz (~70 mesh) and placed between layers of quartz wool within the quartz tube reactor, forming a sandwich layer. Above the quartz wool, quartz sand with a size of approximately ~70 mesh and a thickness of 5 cm was loaded to facilitate substrate evaporation. Before the catalytic evaluation, the α-MoC-based catalyst was pre-treated in the mixed flow of CH_4 and H_2 (15% CH_4 and 85% H_2 in volume, 30 mL/min). The catalyst was heated to 863K at a rate of 5 K min^{-1} and held at 863K for 2 hours then naturally cooled down to room temperature. For the catalytic tests, the catalyst was firstly heated up to the desired temperatures under the protection of carrier gas (60 mL/min, 5% Ar as internal standard in 95% N_2). The liquid mixture of ethanol and water was then pumped into the pre-evaporating chamber (at 423K) located on top of the reactor by a high-performance liquid chromatography pump. The liquid products and unreacted ethanol were collected by a condenser connected to a circulating condensing system operating at 278K. The composition of the liquid product was determined using a 1,4-dioxane external standard method by gas

chromatography (Agilent 7820). The gas product (H_2, CO, CO_2, CH_4, C_2H_4, C_2H_6) and carrier gas were analyzed by online gas chromatography (Agilent 6890).

The carbon balance, δ_C was determined according to the following equation, mainly based on the total amount of carbon in and out of the reactor.

$$\delta_C = \frac{2n_{\mathrm{EtOH,out}} + \sum n_{i,\mathrm{out}} \cdot N_{C,i}}{2n_{\mathrm{EtOH,in}}} \cdot 100\%$$

Where $n_{\mathrm{EtOH,in}}$ and $n_{\mathrm{EtOH,out}}$ are the averaged inlet and outlet ethanol molar flows, $n_{i,\mathrm{out}}$ and $N_{\mathrm{C},i}$ are the molar flow and the number of carbon atoms in product *i*, respectively. The values exceeding 100% may be attributed to minor inaccuracies in controlling the ethanol inlet flow, leading to a slightly higher ethanol input than anticipated.

The long-term stability evaluation of 3Pt3Ir/α-MoC for selective steam reforming of ethanol and water was conducted at atmospheric pressure using the same reactor employed for catalytic performance tests. The analysis of both gas and liquid phase products was carried out every 2 hours.

Characterization of catalysts

XRD.

X-ray Diffraction patterns were collected on a Rigaku X-ray diffractometer operated at 40 kV and 100 mA, using Cu K_α radiation.

All the samples were pre-activated in a mixture of 15% CH_4/H_2 at 863 K for 2 hours and carefully sealed in a sample holder under argon protection in a glove box before measurement.

XAFS.

Pt L_3 edge and Ir L_3 edge X-ray absorption fine structure (XAFS) spectra measurements were carried out at the BL39XU beamline of the SPring-8 in Japan and and Beijing Synchrotron Radiation Facility. All the samples were pre-activated in a mixture of 15% CH_4/H_2 at 863 K for 2 hours and carefully sealed under argon protection in a glove box. Pt foil, PtO_2, Ir foil and IrO_2 were used as standards for calibration.

All XAFS spectra were processed using the Ifeffit package version 1.2.11 (*4*). The extended XAFS oscillation was fitted according to a back-scattering equation, using FEFF models (*5*) generated from crystal structures of Pt foil and Ir foil. The error bars of coordination number are calculated based on fitting results generated.

STEM.

Aberration-corrected STEM imaging and EELS mapping were performed on a Nion HERMES-100 under an accelerating voltage of 100 kV. All the samples were pre-activated in a mixture of 15% CH_4/H_2 at 863 K for 2 hours and then naturally cooled down to room temperature and passivated in 0.5% O_2 in Ar (30 ml/min) overnight. The passivated sample powders were embedded in resins and then thinned to slice approximately 30 nm thick by ultramicrotomy. Both atomic resolution imaging and spectroscopy experiments were conducted with a convergence semi-angle of 30 mrad. The collection angles for bright field (BF) and annular dark field (ADF) imaging were 0-15 and 92-210 mrad, respectively. The collection angle for EELS mapping was 0-92 mrad. A high beam current of 157 pA was applied to achieve single-atom sensitivity in the STEM-EELS measurements. The absolute values and dispersion in EELS spectra were calibrated by the Si-K signals from the resin and Mo-L signals from α-MoC. The calibrated energy dispersion was 0.774 eV/ch. To visualize individual Pt and Ir atoms on the α-MoC support, the EELS data was further processed using principle component analysis (PCA) with a DigitalMicrograph plug-in (Multivariate Statistical Analysis (MSA), HREM Research Inc.) (*6*), which is a commonly used

denoising algorithm for spectroscopy dataset. Since the pixel size used in EELS mapping was only 1.5 Å, smaller than the bond lengths of Pt(Ir)-Pt(Ir) measured by EXAFS, the Pt-M or Ir-M signals confined to signal pixels can be regarded as isolated Pt or Ir atoms.

3D reconstruction.

ADF-STEM Data acquisition

Tomographic tilt series of 3Pt3Ir/α-MoC and 3Pt/α-MoC were acquired using an aberration-corrected FEI Titan Themis G2 300 microscope (Figs. S11-12). Images were collected in ADF scanning mode at 300 kV. To minimize the sample drift, three sequential images were obtained with a dwell time of 3μs at each tilt angle. To monitor any potential damage, we compared images taken at 0° before, during and after tilt series, indicating the samples were structural stable throughout the tilt experiment (Fig. S13). The total electron dose of each tilt series was estimated to be between 2.3×10^5 electrons $Å^{-2}$.

Image pre-processing and 3D reconstruction

Three images at each tilt angle were registered using normalized cross-correlation and averaged to correct linear sample drift and scan distortion. The drift-corrected images were denoised using the block-matching and 3D filtering (BM3D) algorithm (*7*). The BM3D parameters were optimized by minimizing the difference between simulated ADF-STEM images and denoised experimental images. After denoising, a 2D mask slightly larger than the boundary of the sample was defined for each experiment image. The background level was estimated using Laplacian interpolation from the background outside the mask. The background-subtracted images were aligned by cross-correlation with forward projection of iterated 3D reconstruction and center of mass method.

After image pre-processing, each tilt series was reconstructed by the Real Space Iterative Reconstruction (RESIRE) algorithm (*8*). The reconstruction converged in 200 iterations. Angular refinement and spatial re-alignment were applied to reduce the angular errors caused by rotation of sample holder and stage.

Determination of 3D atomic coordinates and chemical species

For each 3D reconstruction, all local maxima were identified. The position of potential atoms was extracted from a local volume of $3.1 \times 3.1 \times 3.1$ $Å^3$ (9×9×9 voxels) around each local maxima with a polynomial fitting method (*9*). A minimum distance constraint of 2.2 Å to neighboring atoms was used to delete non-atom positions. After manually correcting a very small fraction of unidentified and misidentified atoms, the final atom positions were defined (*10*).

All potential atoms were initially classified into three different categories (non-atom, Mo and Pt/Ir atoms) by applying one-dimension k-mean clustering method (*11*). Initial classification models were refined by atom-flipping method and local reclassification method (*12*). We manually checked a small percentage of the inconsistent and misclassified atoms.

Calculation of mean bond length and coordination number

We calculated the total radial distribution function (RDF) of atomic model and pair distribution function (PDF) of Pt/Ir-Pt/Ir, Pt/Ir-Mo and Mo-Mo atom pair. The first peak of RDF and PDF were fitted to a Gaussian distribution function to get mean bond length. The coordination number of Pt/Ir atoms was calculated by counting the surrounding atom number with the first valley distance in PDF as cutoff distance (Figure 2G-H).

Mechanism study

Near-Ambient-Pressure X-ray Photoelectron Spectroscopy (NAP-XPS).

The *NAP-XPS* analysis was performed on the ambient pressure photoelectron spectroscopy (APPES) end station at BL02B01 in the Shanghai Synchrotron Radiation Facility (SSRF, 3.5 GeV). The catalyst was pre-activated in a mixture of 15% CH_4/H_2 at 863 K for 2 hours and pressed into small pellets (6 mm diameter) in a glove box and placed on the sample holder. The sample was then carefully transferred into the analysis chamber and tested in an ultra-high vacuum. After the measurement, the mixed gas of ethanol/water was introduced into the analysis chamber by a leak valve. After the pressure of gas reached a constant value, the temperature of the sample was raised up to a target value and the reaction *in-situ* proceeded for 1 hour. The signals of C 1s, O 1s, Mo 3d, Pt 4f and Ir 4f were then acquired. The pressure of gas and temperature of sample were changed to observe the evolution of surface species.

Transient kinetic analysis.

TKA system is consisted of two identical tubes: the reactor tube and the bypassing tube (see Fig. S18 for experimental setup) (*13*). 20 mg passivated 3Pt3Ir/α-MoC was loaded in the reactor tube and the bypassing tube was empty. After pretreatment at 863 K, the system was cooled down to 323 K under 20 sccm Ne and the reactant gas (20 sccm Ar/C_2D_5OD=19.5/0.5) was purged into the bypassing tube and detected by the MS until the signals were stable (step i). Then the downstream four-way valve was switched and the outflow from the reactor tube was detected by MS (step ii). Finally, a switch from 20 sccm Ne to 20 sccm reactant gas in the reactor tube was performed quickly with little pressure fluctuation (step iii) and the transient signals were recorded by online MS.

***In-situ* DRIFTS.**

In-situ diffuse reflectance Fourier transform infrared spectroscopy (in-situ DRIFTS) was performed in an in-situ reaction cell on a VERTEX 70 spectrometer equipped with an MCT narrow-band detector, with a resolution of 4 cm^{-1} (*14*). Firstly, the catalyst was pressed into the cell and in-situ reduced with mixed flow of CH_4 and H_2 at 863K for 2h, then switched to Ar to clean all residual CH_4 and H_2 and naturally cooled down to desired temperatures. After the baseline was collected, the gas phase ethanol (or mixture of water and ethanol) was bubbled in the cell with Ar. The spectra were collected every 30 seconds until all the peaks went to stable. Once the adsorption/reaction was completed, the inlet flow was switched to pure argon and the desorption spectra of ethanol were then recorded.

DFT calculations

Calculation Methods.

All spin polarization calculations were performed using the Vienna Ab Initio simulation package (VASP) (*15, 16*). The electron-ion interaction was described with the projector augmented wave (PAW) method (*17, 18*). The electron exchange and correlation energies were treated within the generalized gradient approximation in the Perdew-Burke-Ernzerhof formalism (GGA-PBE) (*19*). The energy cutoff of plane wave basis was set to 450 eV, electron smearing width of σ = 0.2 eV was employed according to the Methfessel-Paxton technique, and the MP k-point sampling was utilized. All transition states were estimated using the Climbing Image Nudged Elastic Band (CI-NEB) method (*20*), and stretching frequency analysis was performed to verify whether a transition state associated with a solely imaginary frequency. The barrier (E_a) and reaction energy (ΔE_r) were calculated according to $E_a = E_{TS} - E_{IS}$ and $\Delta E_r = E_{FS} - E_{IS}$, where E_{IS}, E_{FS} and E_{TS} are the total energy of the corresponding initial state (IS), final state (FS) and transition state (TS), respectively.

Calculation Models.

The calculated lattice constant of cubic Pt cell (fcc) is 3.919 Å (experimental = 3.924 Å), and the Pt-Pt bond is 2.771 Å. The calculated lattice constant of cubic MoC cell (fcc) is 4.332 Å (experimental = 4.270 Å), and the Mo-Mo bond is 3.063 Å. In top views of five surface models for α-MoC(111), Pt(111), Pt(210), Pt_1/α-MoC (111) and Ir_1/α-MoC (111), the unit cell p(3×3) was used for α-MoC(111) and Pt(111), the unit cell p(2×2) was used for Pt(210), the unit cell p(4×4) was used for Pt_1/α-MoC (111) and Ir_1/α-MoC (111), and the same 3×3×1 k-point sampling were used for all these models. Totally, MoC(111) surface has 27 Mo and 27 C atoms, in which 9 Mo and 18 C were fixed; the Pt(111) has 64 Pt atoms, and 32 Pt were fixed; the Pt(210) has 40 Pt atoms, and 12 Pt were fixed; the Pt_1/MoC(111) and Ir_1/α-MoC (111) hava 1 Pt/Ir, 48 Mo and 48 C atoms, in which 16 Mo and 32 C were fixed, the Pt/Ir coverage was 1/16.

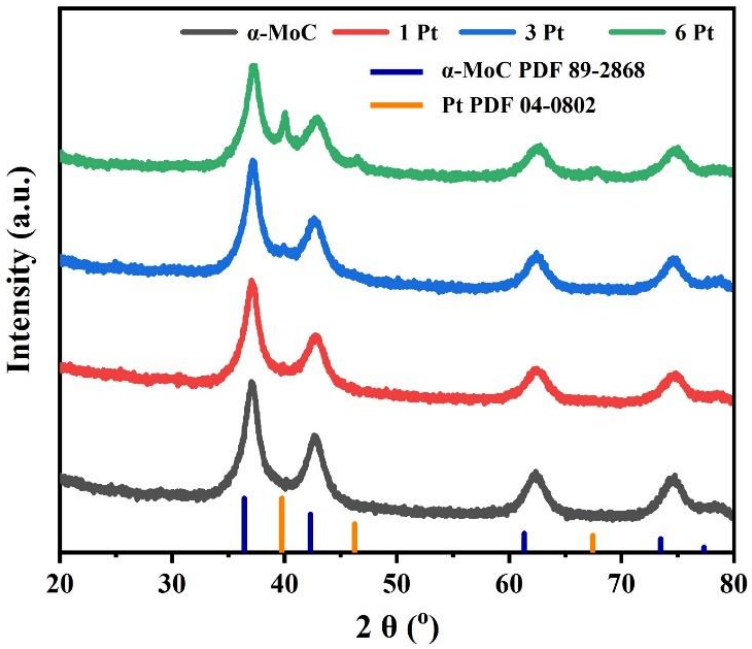

Fig. S1.

Crystal structure of Pt/α-MoC. XRD patterns of α-MoC supported Pt with different metal loadings.

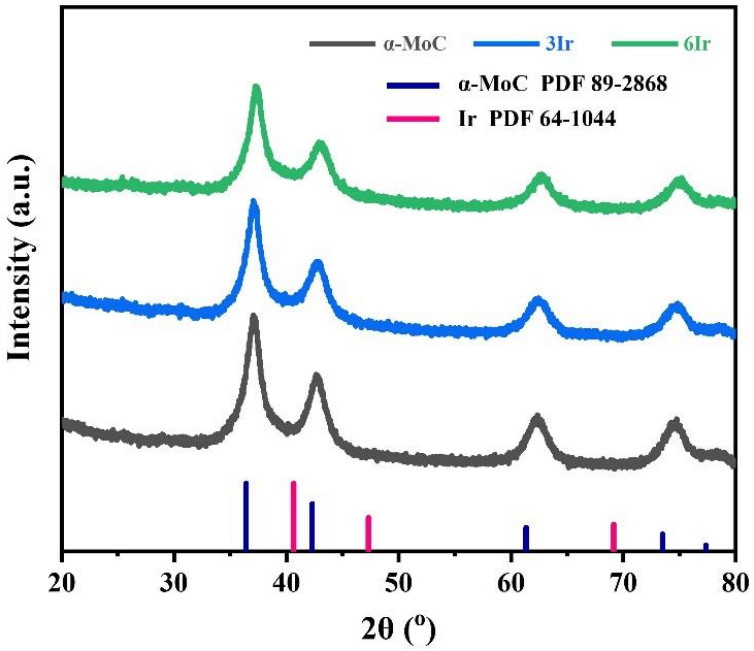

Fig. S2.

Crystal structure of Ir/α-MoC. XRD patterns of α-MoC supported Ir with different metal loadings.

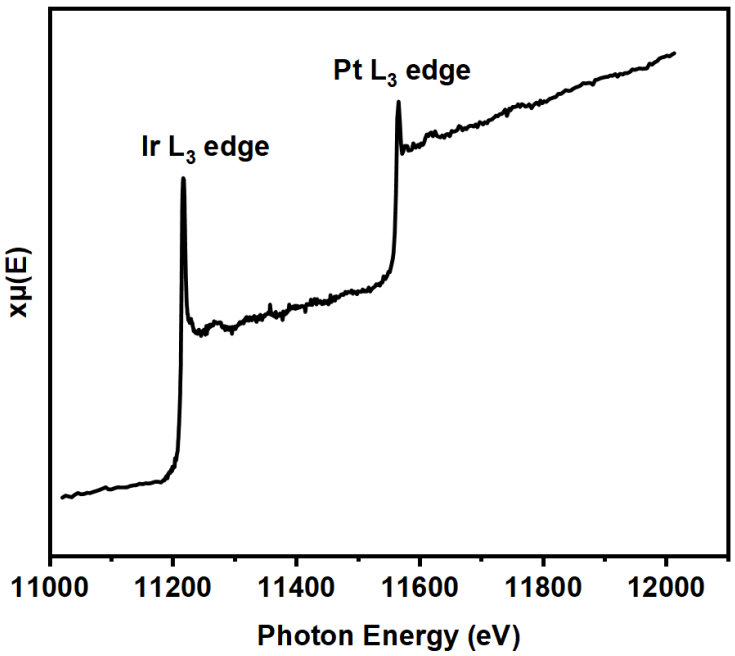

Fig. S3.

Overlapping of Pt and Ir adsorption edge. XAS of Pt/Ir L_3-edge of an oxidized 1Pt1Ir/α-MoC catalyst in conventional total fluorescence detection mode.

Note:

This sample is presented here simply to illustrate the challenge of measuring the XAS of Pt/Ir bimetallic materials. Due to the adjacent absorption L_3 edge of Pt and Ir (11564 eV and 11215 eV, respectively), common measurement methods including transmission and total fluorescence detection mode will result in a spectrum with overlapping signals for PtIr/α-MoC, which restrains the analysis of extended edge. Alternatively, we were able to divide the absorption edge of these two neighboring elements with identical concentrations by separating the emitting fluorescence, from which the local coordination environment information could be extracted in high energy-resolution fluorescence detection mode (HERFD).

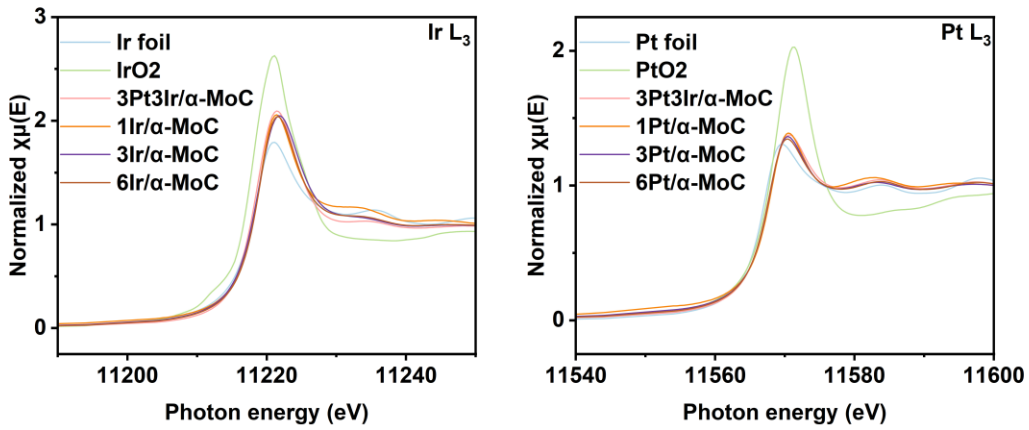

Fig. S4.

Near-edge information. Normalized XANES spectra of for α-MoC supported PtIr catalysts at Ir L_3-edge and Pt L_3-edge. The Pt and Ir within the catalysts do not exhibit significantly different valence states.

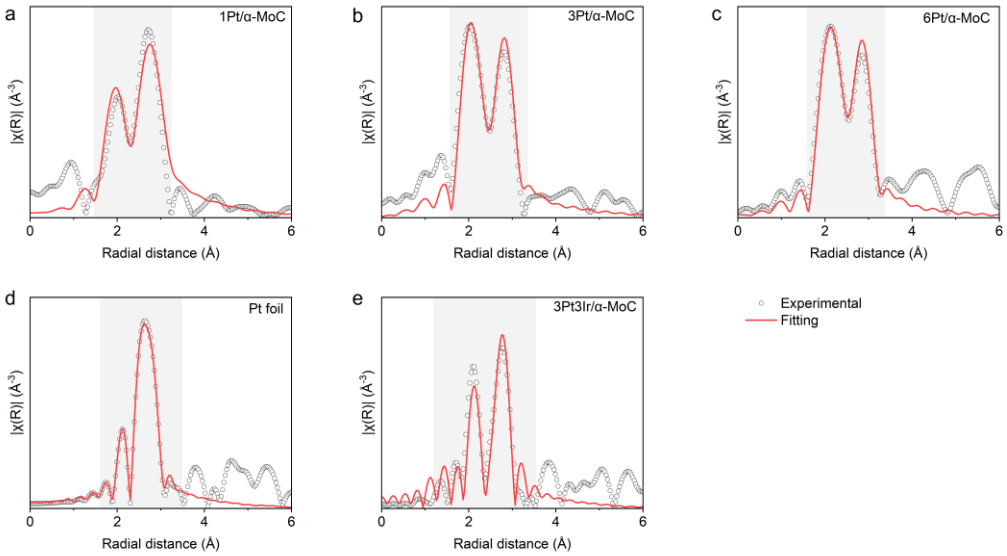

Fig. S5.

Pt EXAFS fitting in R space. EXAFS and the fittings curves of Pt L_3-edge in R-space for 1Pt/α-MoC (a), 3Pt/α-MoC (b), 6Pt/α-MoC (c), Pt foil (d), and 3Pt3Ir/α-MoC (e). Fitting region is noted with grey shadow.

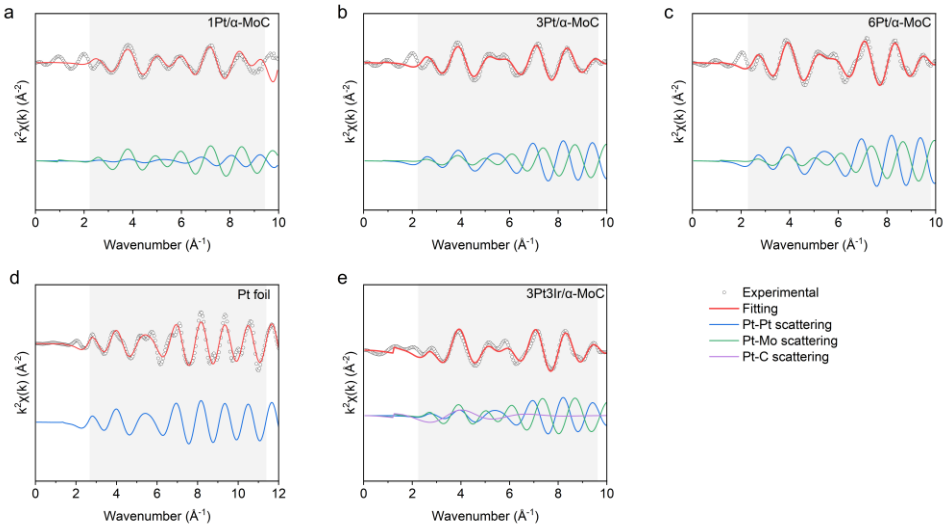

Fig. S6.

Pt EXAFS fitting in k space. EXAFS functions and the fitting curves along with scattering paths of Pt L_3-edge in k^2-space for 1Pt/α-MoC (a), 3Pt/α-MoC (b), 6Pt/α-MoC (c), Pt foil (d), and 3Pt3Ir/α-MoC (e). Fitting region is noted with grey shadow.

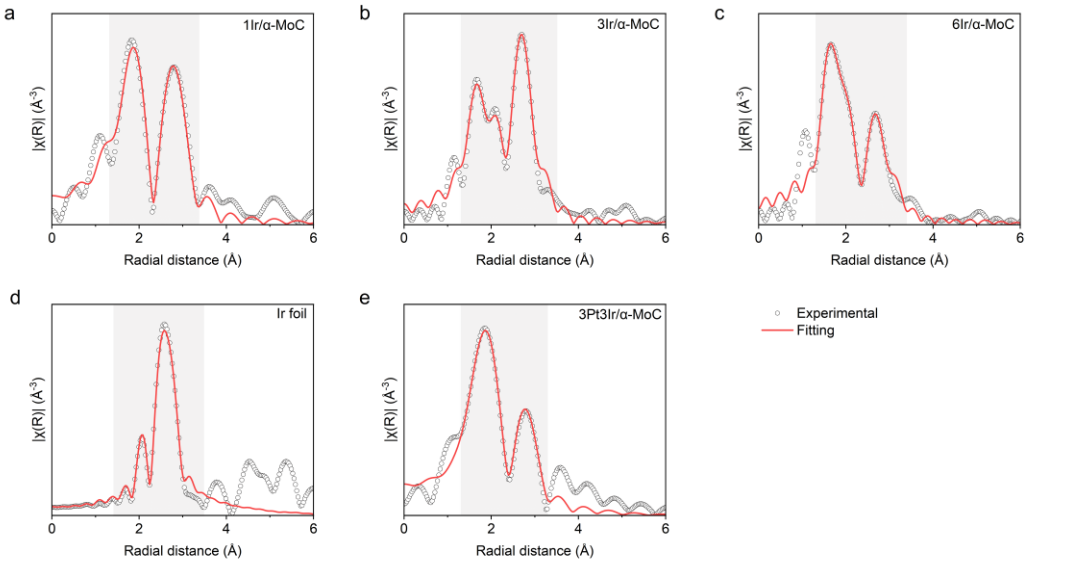

Fig. S7.

Ir EXAFS fitting in R space. EXAFS functions and the fitting curves of Ir L_3-edge in R-space for 1Ir/α-MoC (a), 3Ir/α-MoC (b), 6Ir/α-MoC (c), Ir foil (d), and 3Pt3Ir/α-MoC (e). Fitting region is noted with grey shadow.

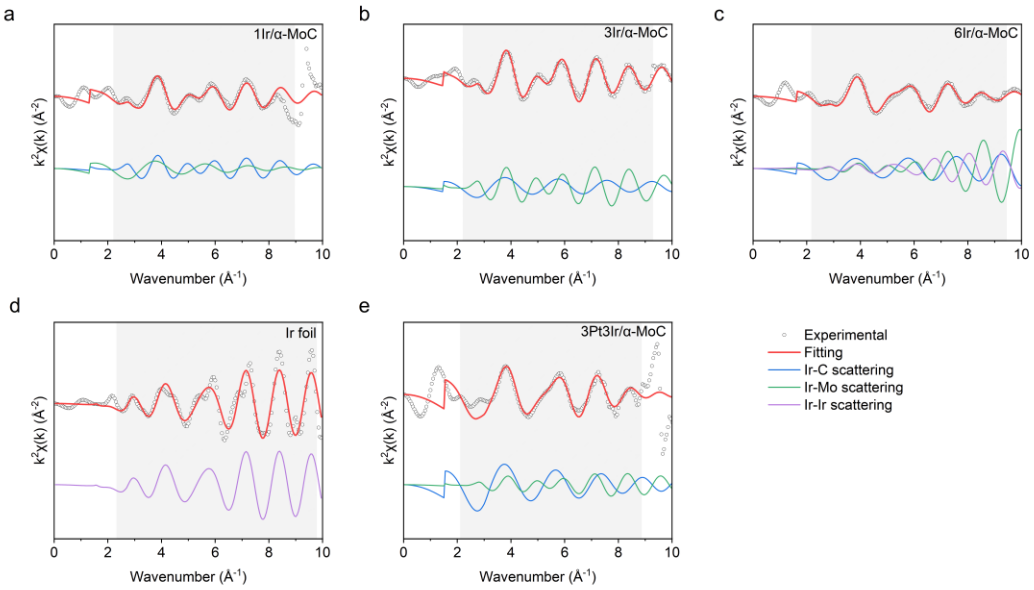

Fig. S8.

Ir EXAFS fitting in k space. EXAFS functions and the fitting curves along with scattering paths of Ir L_3-edge in k^2-space for 1Ir/α-MoC (a), 3Ir/α-MoC (b), 6Ir/α-MoC (c), Ir foil (d), and 3Pt3Ir/α-MoC (e). Fitting region is noted with grey shadow.

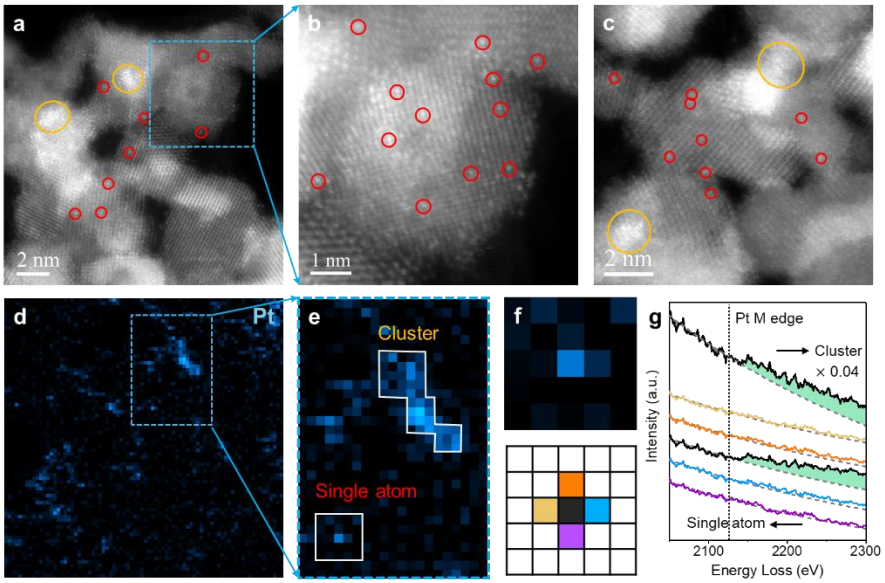

Fig. S9.

The supplementary STEM images and elemental analysis of 3Pt/α-MoC. High-magnification STEM-HAADF image (a) and a zoom-in image from the region highlighted by a dashed square (b). Some of the Pt clusters and atomic Pt_1 species were highlighted by the yellow circles and red circles, respectively. Additional ADF figures of 3Pt/α-MoC are added in Fig. S10. (c-g) Atomic-scale EELS mapping on 3Pt/α-MoC. (c) ADF image and (d) the corresponding elemental map of Pt. (e) Pt Elemental map enlarged from a blue rectangle in (d). A Pt single atom and a Pt cluster are highlighted. The pixel size used for the EELS mapping is 0.15 nm, so that the signal from a single Pt is confined within a single pixel (*21*). A representative example of Pt single atoms is denoted by a white square in (e). (f) The elemental map and the corresponding pixel indexes of the Pt single atom in (e). (g) EELS spectra extracted from the single atom and cluster of Pt shown in (e) and (f), the spectra share the same color code with the corresponding pixel in (e). The gray dashed lines are the fitted background for the EELS spectra.

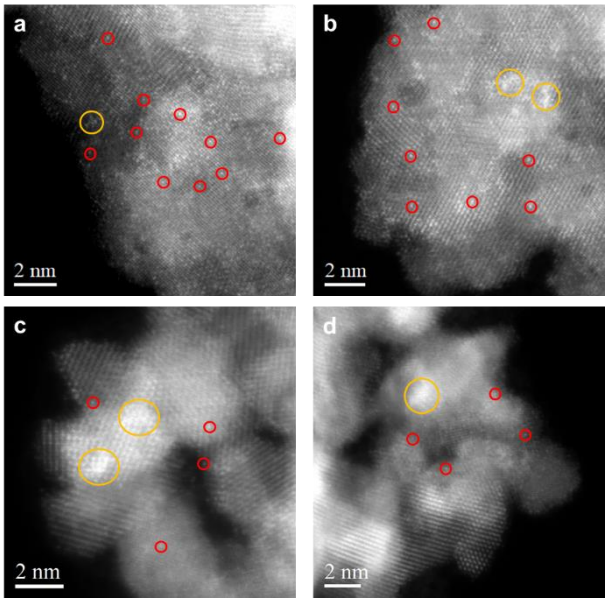

Fig. S10.

The supplementary STEM-ADF images of 3Pt3Ir/α-MoC and 3Pt/α-MoC catalysts. (a-b) 3Pt3Ir/α-MoC and (c-d) 3Pt/α-MoC. (Single atoms of Pt/Ir noted by red circle, and clusters noted by yellow circle)

Fig. S11.

Tomographic tilt series of 3Pt3Ir /α-MoC nanoparticle. 56 HAADF-STEM images with a tilt range from −73.0° to +71.5°. The value of angle to which the image belongs is recorded in the upper right corner of each image. Scale bar, 2 nm.

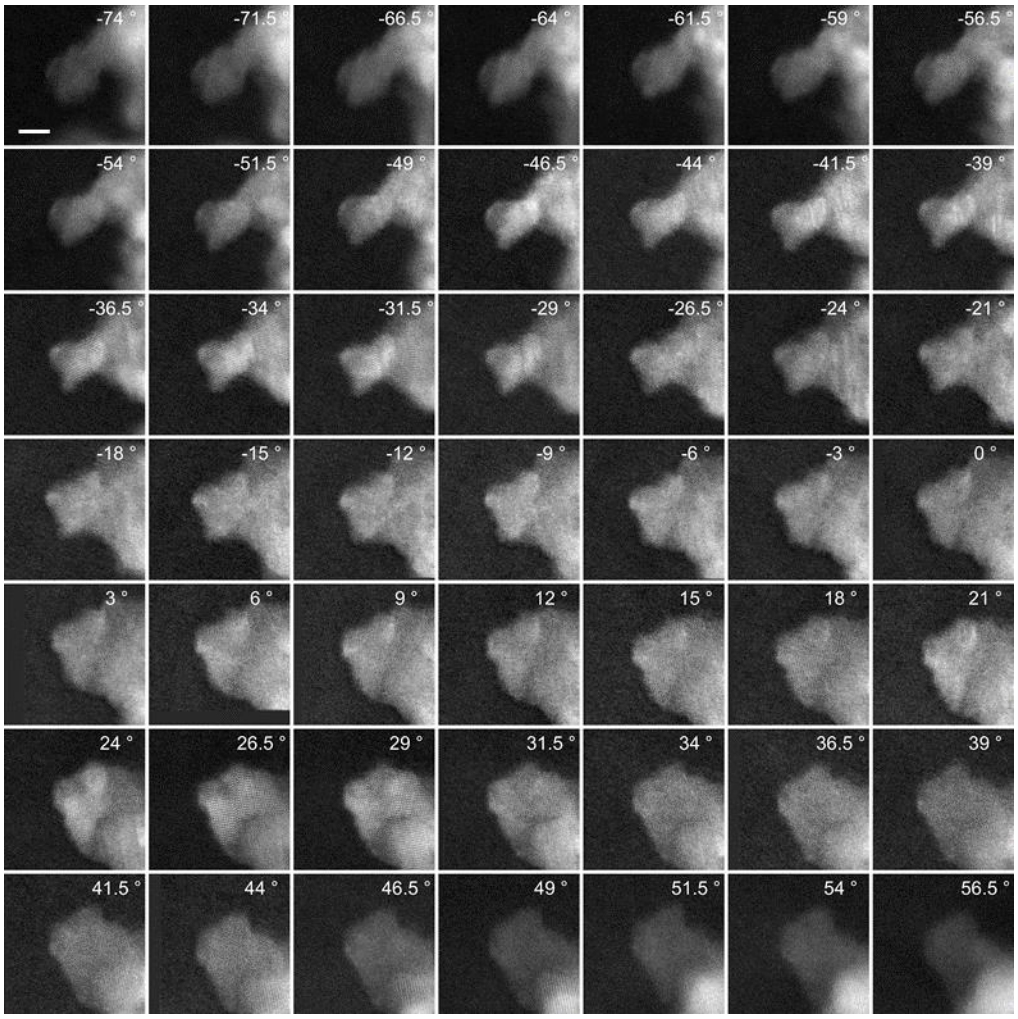

Fig. S12.

Tomographic tilt series of 3Pt/α-MoC nanoparticle. 49 HAADF-STEM images with a tilt range from −54.0° to +74°. The value of angle to which the image belongs is recorded in the upper right corner of each image. Scale bar, 2 nm.

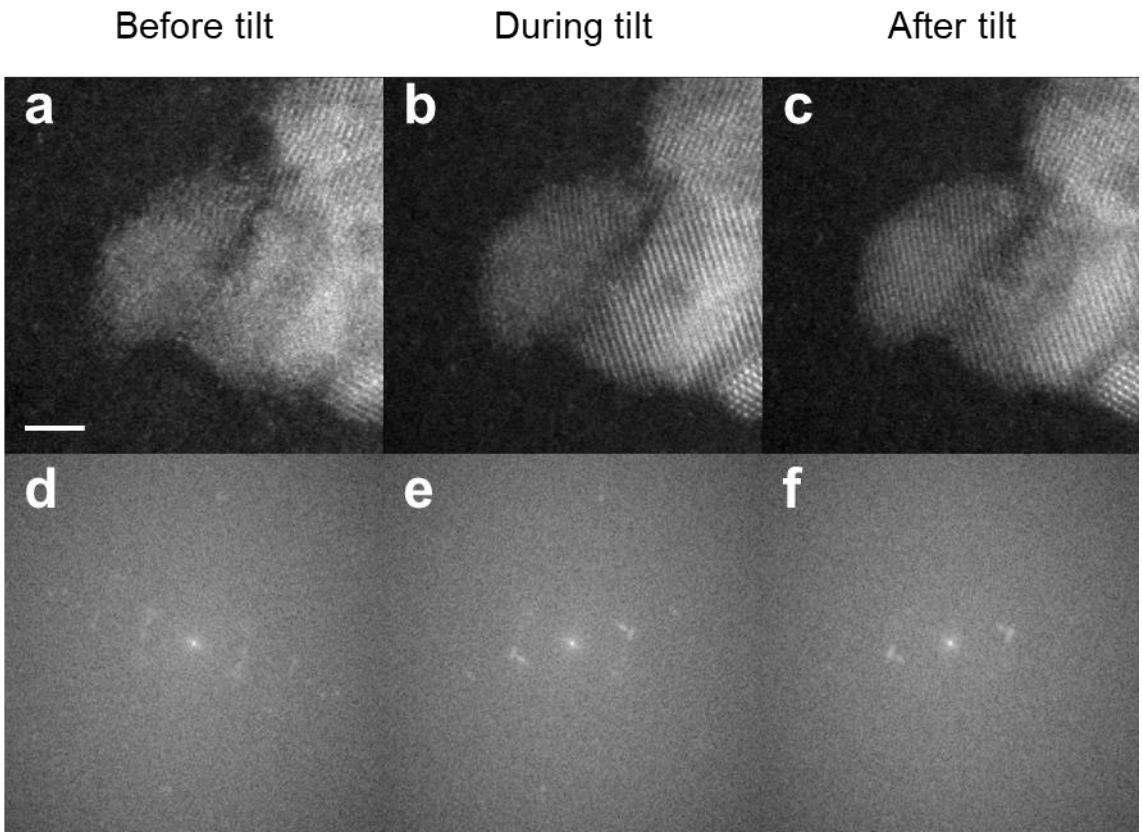

Fig. S13.

Consistency check of 3Ir3Pt/α-MoC nanoparticles. 0° projection images of 3Ir3Pt/α-MoC (a-c) and corresponding FFT images (d-f) before, during and after tilting experiments. Scale bar, 2 nm.

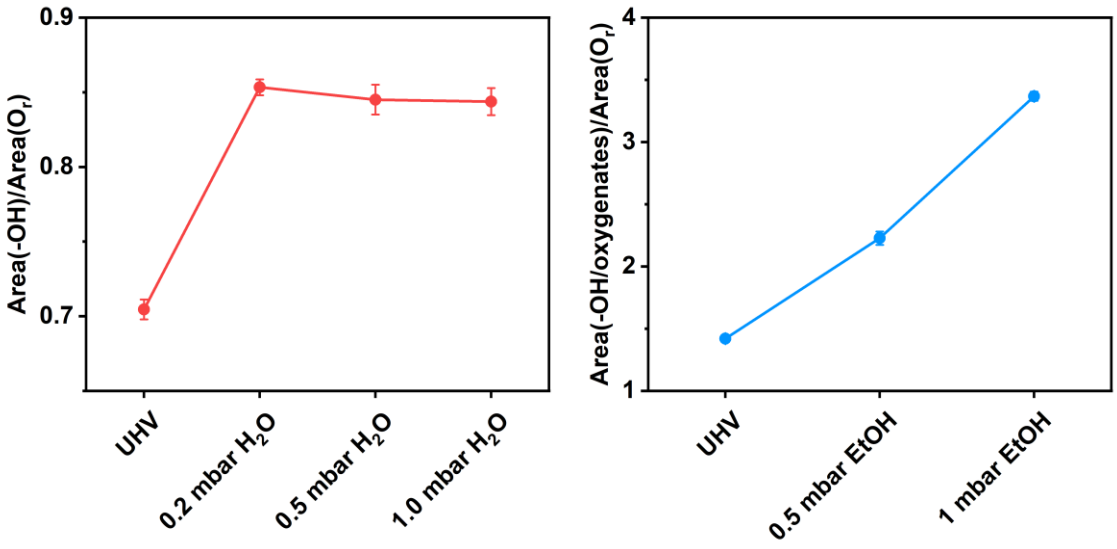

Fig. S14.

Surface species quantification on 3Pt3Ir/α-MoC. Ratio of surface -OH/oxygenate species to residual oxygen, calculated from O 1s peak fitting (Figs. 3A-B) under H2O or ethanol gas exposure. The error bars are calculated based on uncertainties from peak fitting of the O 1s signal and the error propagation formula.

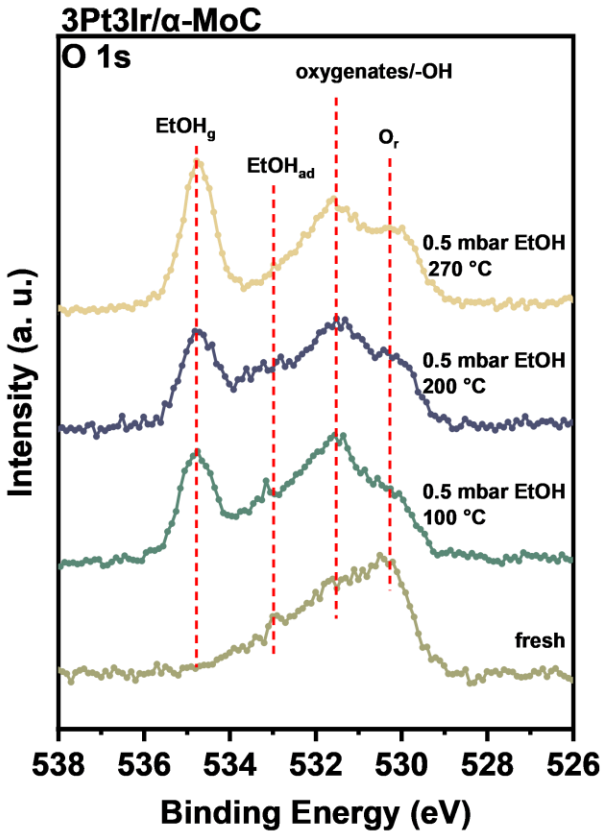

Fig. S15.

Evolution of surface oxygen species during ramping process in ethanol. The *NAP-XPS* results (O 1s) of 3Pt3Ir/α-MoC catalyst under 0.5 mbar ethanol at different temperatures. The O-H bond of ethanol was dissociated at room temperatures on the surface of 3Pt3Ir/α-MoC, generating active oxygenates/-OH groups (*22*). And massive amount of adsorbed ethanol was converted to oxygenates/-OH groups with the elevated temperatures.

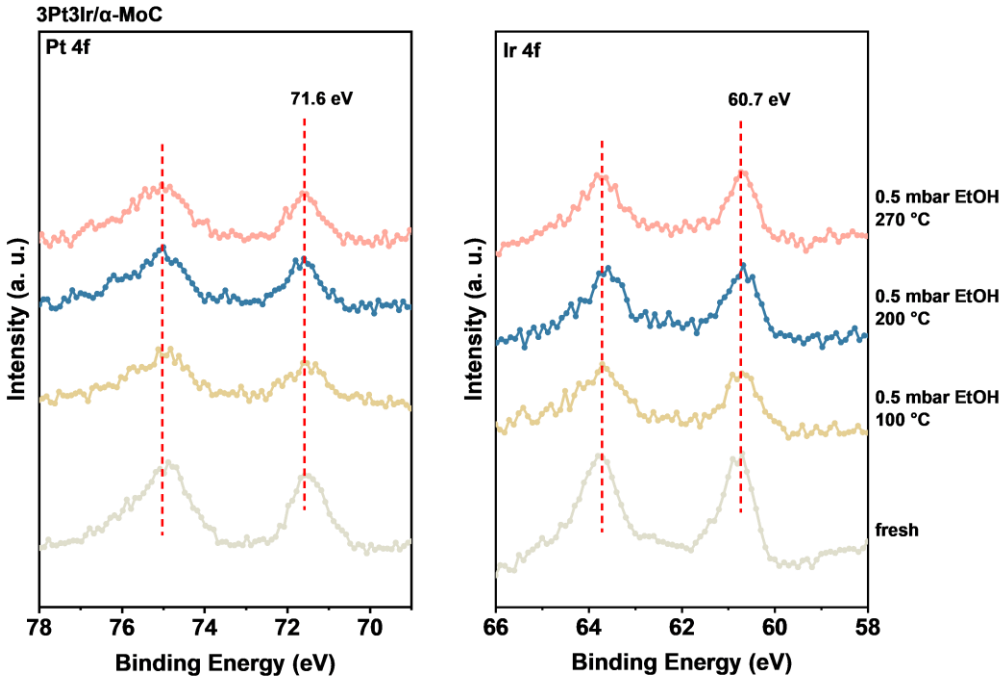

Fig. S16.

Evolution of supported metal species during ramping process in ethanol. The *NAP-XPS* results (Pt 4f, Ir 4f) of 3Pt3Ir/α-MoC catalyst under 0.5 mbar ethanol at different temperatures.

Note:

The binding energies of Pt 4f and Ir 4f didn't changed with the elevated temperature at the presence of ethanol, which indicate the generated OH^*/EtO^* groups on the surface of catalysts might bonded to α-MoC rather Pt or Ir species. The slightly positive charged Pt and Ir species also show the partial electron transfer from metals to support and the strong metal-support interaction effect.

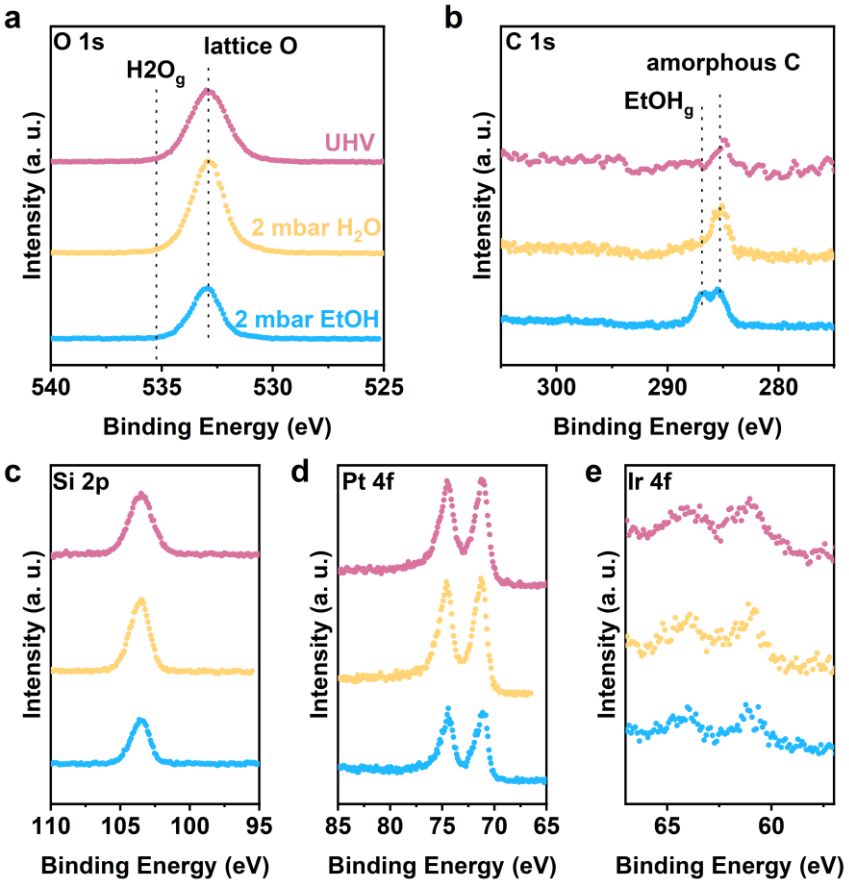

Fig. S17.

Evolution of surface species on 3Pt3Ir/SiO$_2$ as reference. *NAP-XPS* results of O 1s (a), C 1s (b), Si 2p (c), Pt 4f (d), Ir 4f (e) on 3Pt3Ir/SiO$_2$ under ultra-high vacuum (pink), 2 mbar of water (yellow) and 2 mbar of ethanol (blue) at room temperature.

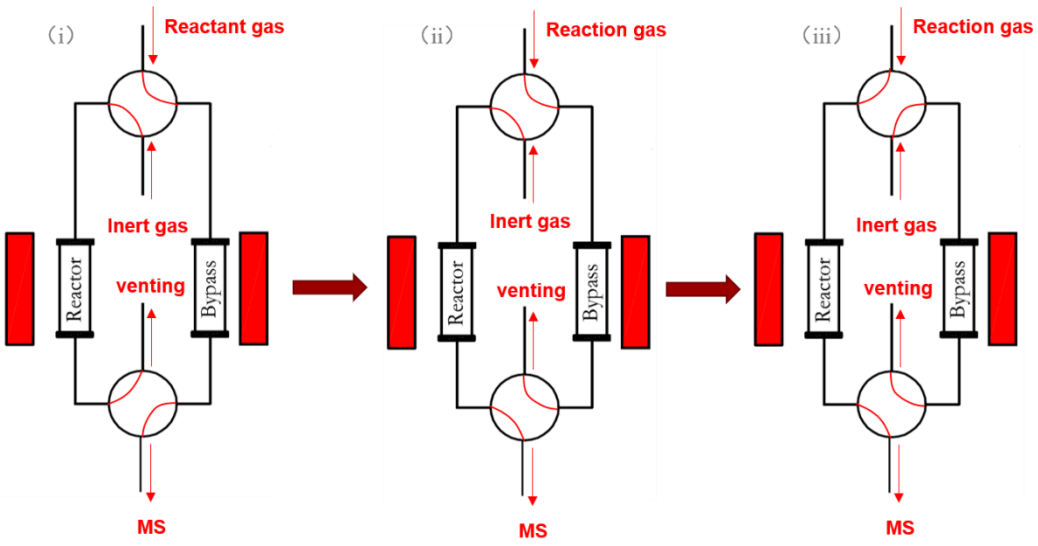

Fig. S18.
Experimental setup for TKA.

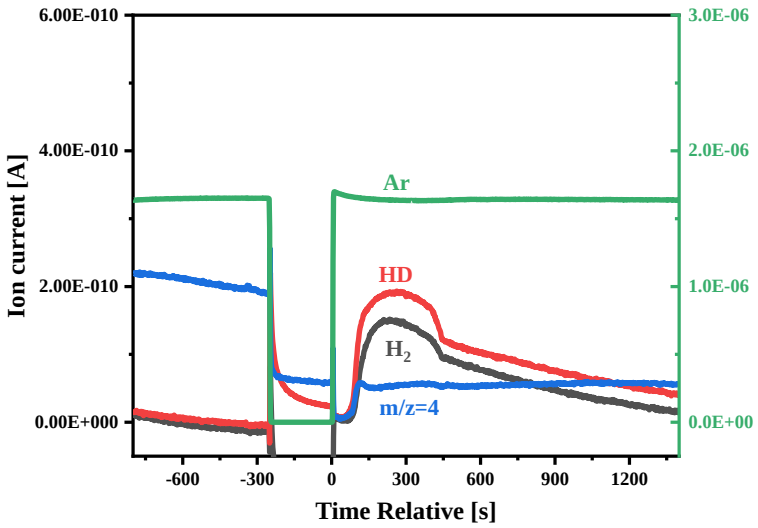

Fig. S19.

Kinetic evidence for ethanol activation on 3Pt3Ir/α-MoC. TKA results for isotopic ethanol (C_2H_5OD) adsorption/reaction on the surface of 3Pt3Ir/α-MoC at room temperatures.

Note:

To further study the dissociation behavior of C-H bond in ethanol, 3Pt3Ir/α-MoC was pre-activated with CD_4 + D_2 to remove the possibly adsorbed or strongly bonded H^* species from the surface of catalyst. The generation of H containing gases (H_2 and HD) indicating the activation of C-H bond in the -CH_2- group of C_2H_5OD at room temperature.

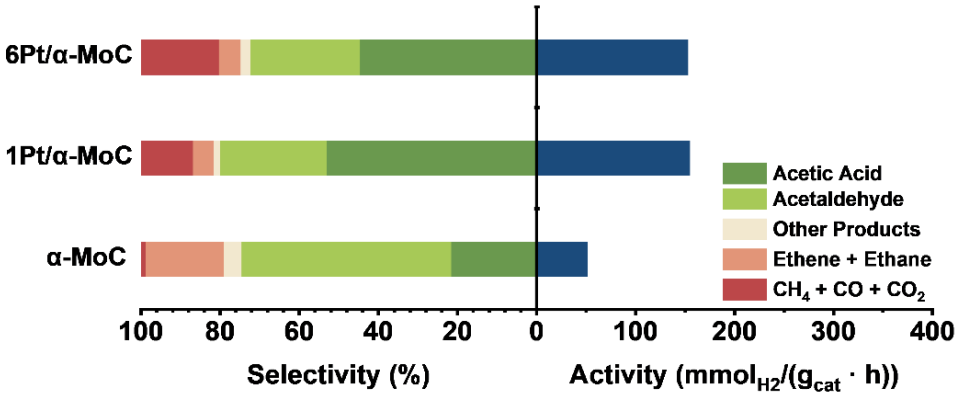

Fig. S20.

Influence of Pt loading on ethanol reforming. The catalytic performance of Pt/α-MoC with different Pt loadings for selective reforming of ethanol with water. Reaction Conditions: 543K, WHSV = 10.6 $g_{ethanol}/(g_{cat} \cdot h)$, carrier gas = 60 mL/min, n (ethanol) : n (H_2O) = 1 : 9.

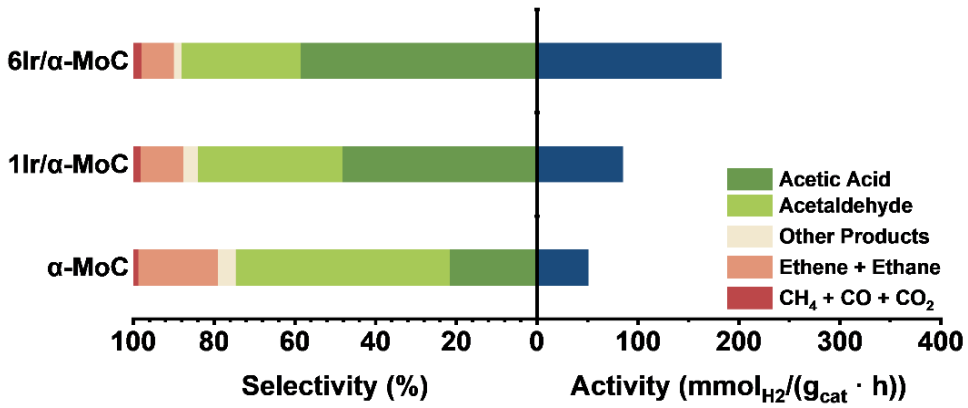

Fig. S21.

Influence of Ir loading on ethanol reforming. The catalytic performance of Ir/α-MoC with different Ir loadings for selective reforming of ethanol with water. Reaction Conditions: 543K, WHSV = 10.6 $g_{ethanol}/(g_{cat} \cdot h)$, carrier gas = 60 mL/min, n (ethanol) : n (H_2O) = 1 : 9.

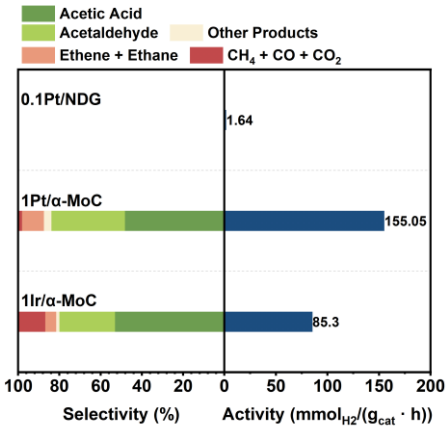

Fig. S22.

Comparison of different atomically dispersed species in ethanol reforming. Comparison of catalytic performance of 1Ir/α-MoC, 1Pt/α-MoC and 0.1Pt/NDG for selective reforming of ethanol with water. Reaction Conditions: 543K, WHSV = 10.6 $g_{ethanol}/(g_{cat} \cdot h)$, carrier gas = 60 mL/min, n (ethanol) : n (H_2O) = 1 : 9.

Note:

1Pt/α-MoC shows higher activity than that of 1Ir/α-MoC, suggesting the intrinsic superiority of Pt-MoC interface comparing to Ir-MoC interface. The atomically dispersed bare Pt on nanodiamond (0.1Pt/NDG, previously reported in ref.(*3*)) shows almost no reforming activity, indicating that Pt single atom cannot catalyze the process, and interfacial structure is essential for ethanol reforming.

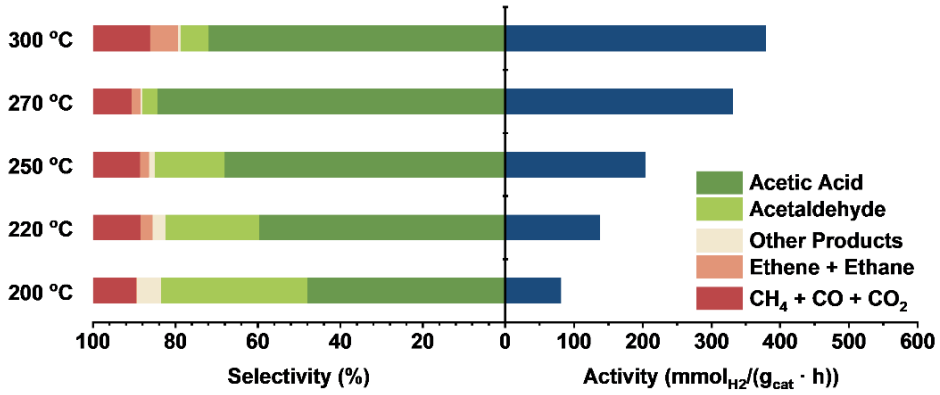

Fig. S23.

Influence of temperature on ethanol reforming. The catalytic performance of 3Pt3Ir/α-MoC for selective reforming of ethanol with water at different reaction temperatures. Reaction Conditions: WHSV = 10.6 $g_{ethanol}/(g_{cat} \cdot h)$, carrier gas = 60 mL/min, n (ethanol) : n (H_2O) = 1 : 9.

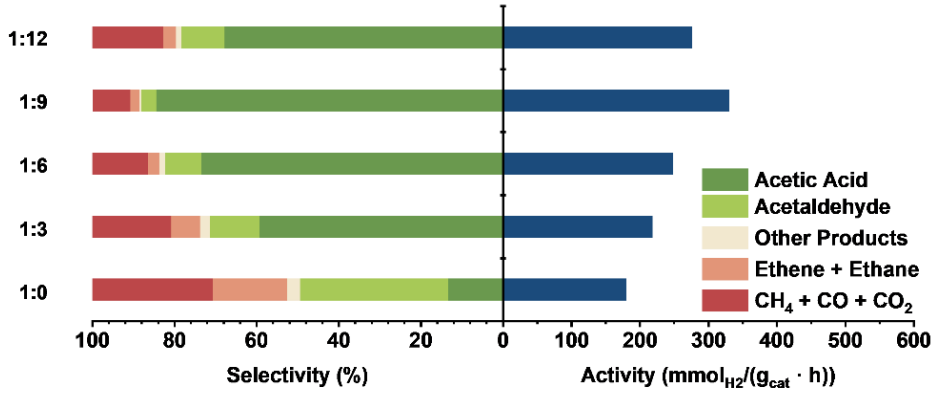

Fig. S24.

Influence of ethanol/water ratio on ethanol reforming. The catalytic performance of 3Pt3Ir/α-MoC for selective reforming of ethanol with water at different ratio of n (ethanol) : n (H_2O). Reaction Conditions: 543K, WHSV = 10.6 $g_{ethanol}/(g_{cat} \cdot h)$, carrier gas = 60 mL/min.

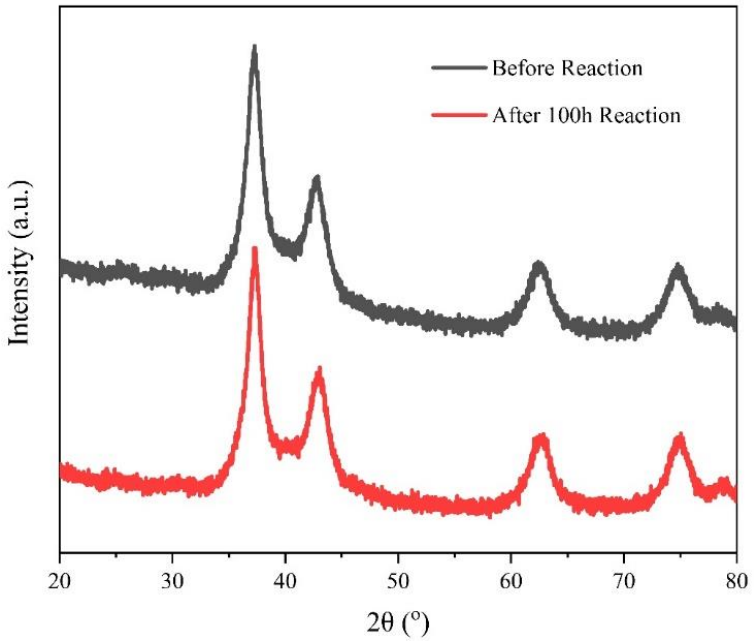

Fig. S25.

Structural stability of 3Pt3Ir/α-MoC during ethanol reforming. XRD patterns of 3Pt3Ir/α-MoC before and after 100 h of reaction. All peaks belong to α-MoC and no obvious peak for Pt or Ir was observed.

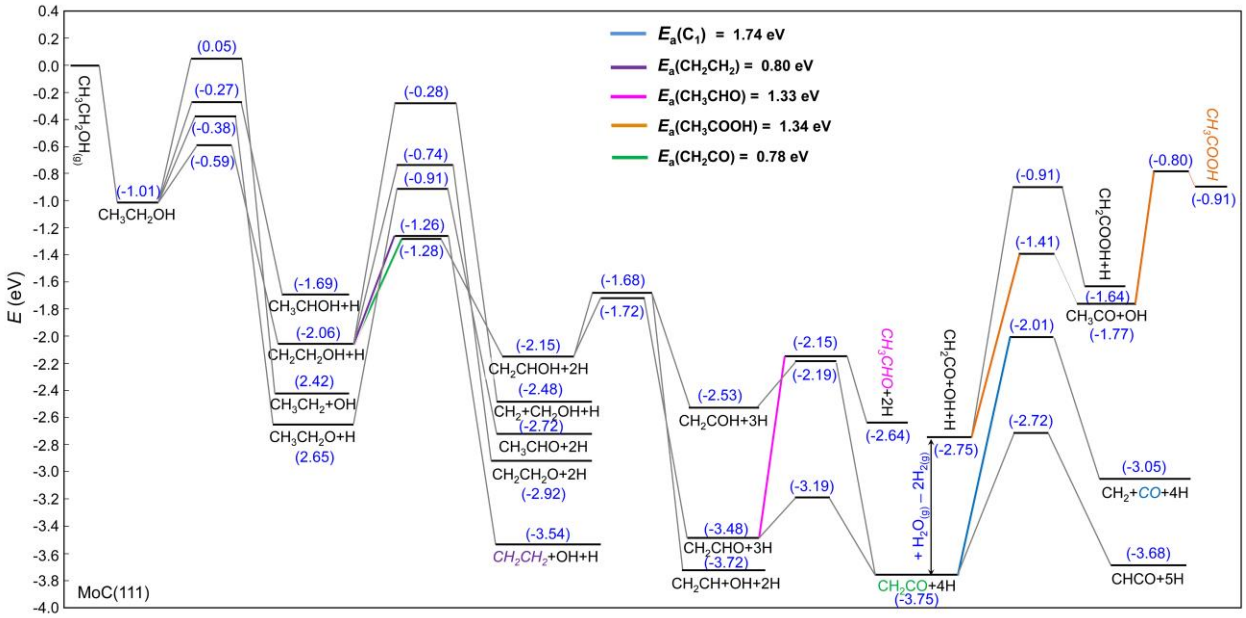

Fig. S26.

Ethanol conversion pathway on α-MoC. The energy profiles of ethanol reforming on pristine α-MoC(111), in which the effective barriers of the different product formation are inserted with the symbol of Ea.

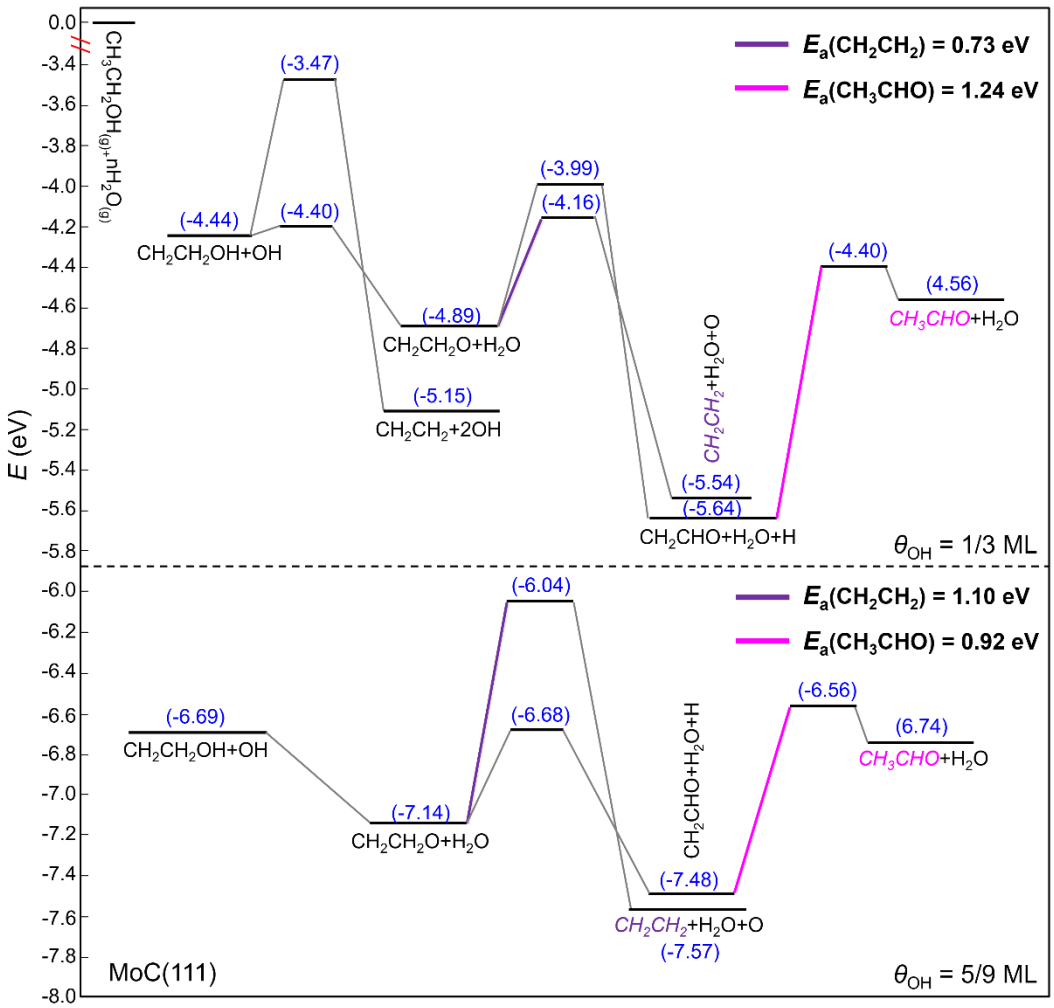

Fig. S27.

Influence of hydroxyl coverage on ethanol conversion pathways on α-MoC. The energy profiles of ethanol reforming on α-MoC(111) at higher hydroxyl coverage of 1/3ML and 5/9 ML, in which the effective barriers of the different product formation are inserted with the symbol of Ea.

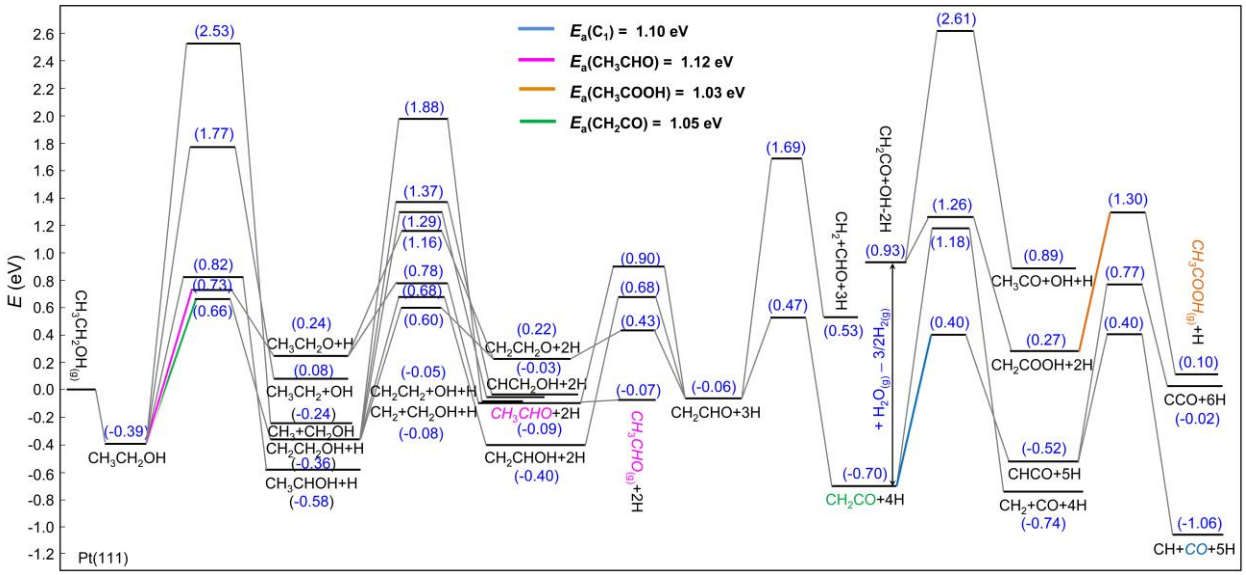

Fig. S28.

Ethanol conversion pathways on Pt(111). The energy profiles of ethanol reforming on Pt(111), in which the effective barriers of the different product formation are inserted with the symbol of Ea.

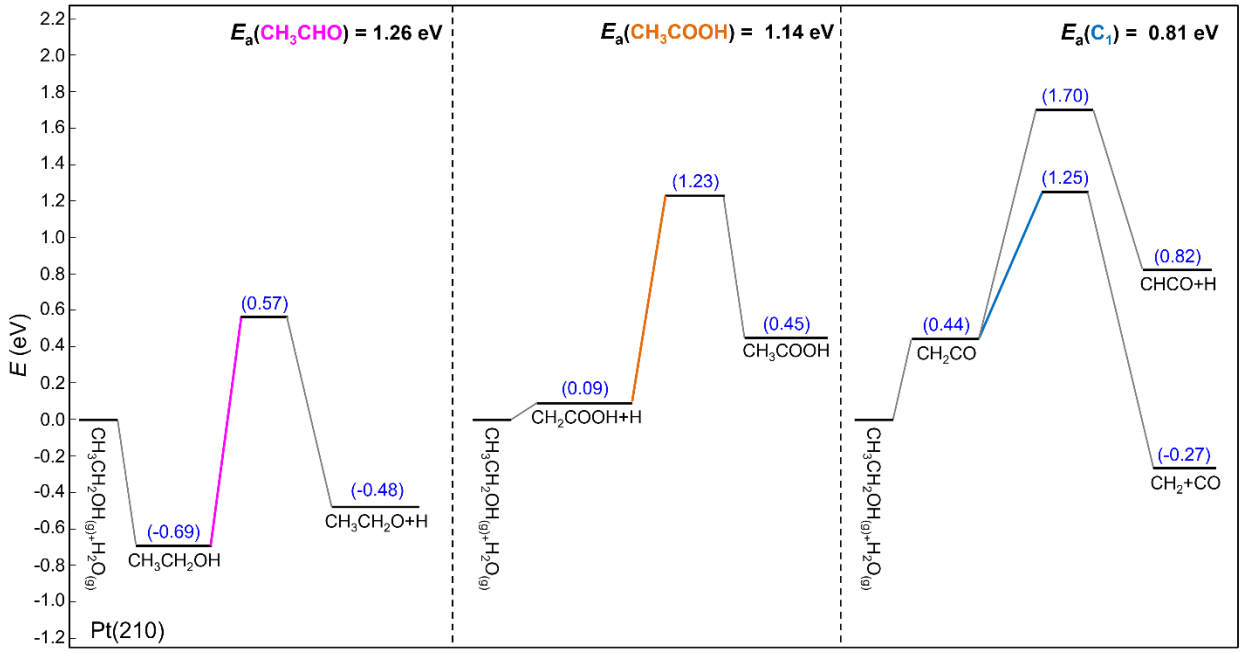

Fig. S29.

Critical ethanol conversion pathways on Pt(210). The energy profiles for the critical steps of acetaldehyde, acetic acid and C_1 products formation in ethanol reforming on Pt(210), in which the effective barriers of the different product formation are inserted with the symbol of Ea

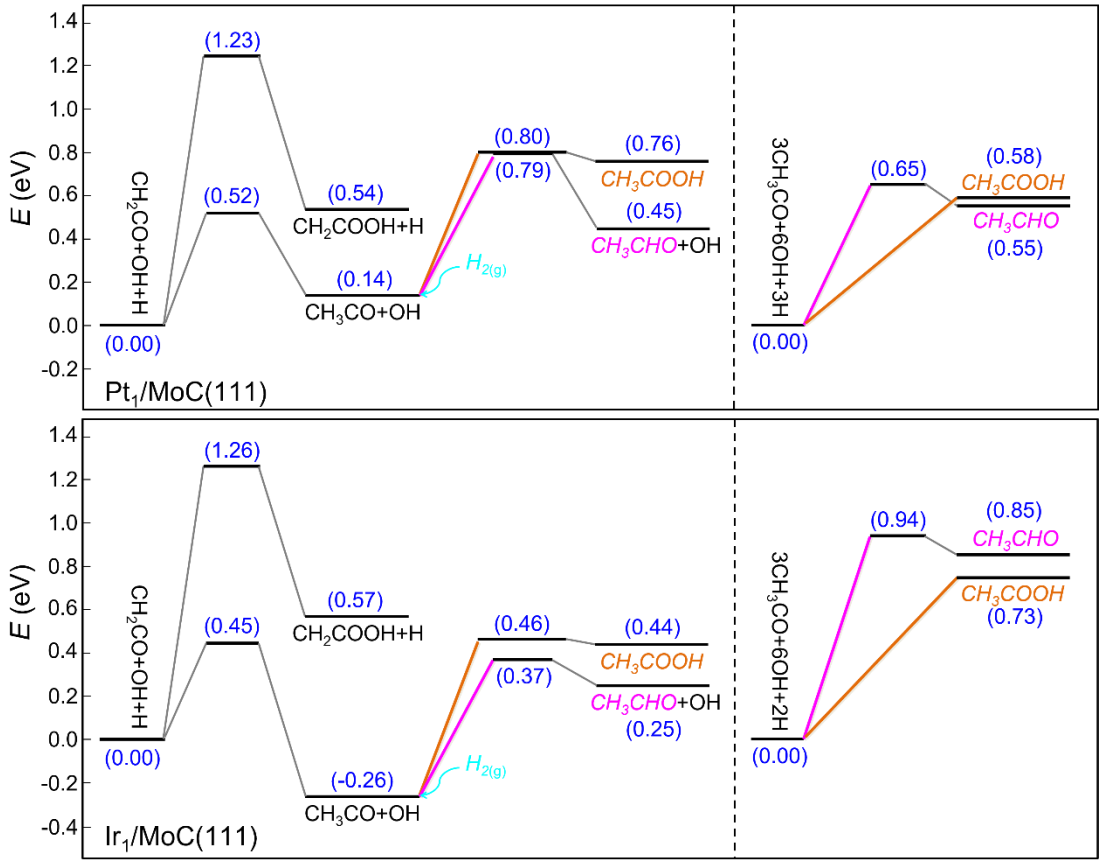

Fig. S30.

Critical pathways for C_2 oxygenates formation on M_1/MoC. The energy profiles for the critical steps of acetaldehyde and acetic acid formation in ethanol reforming on Pt_1/MoC(111) and Ir_1/MoC(111).

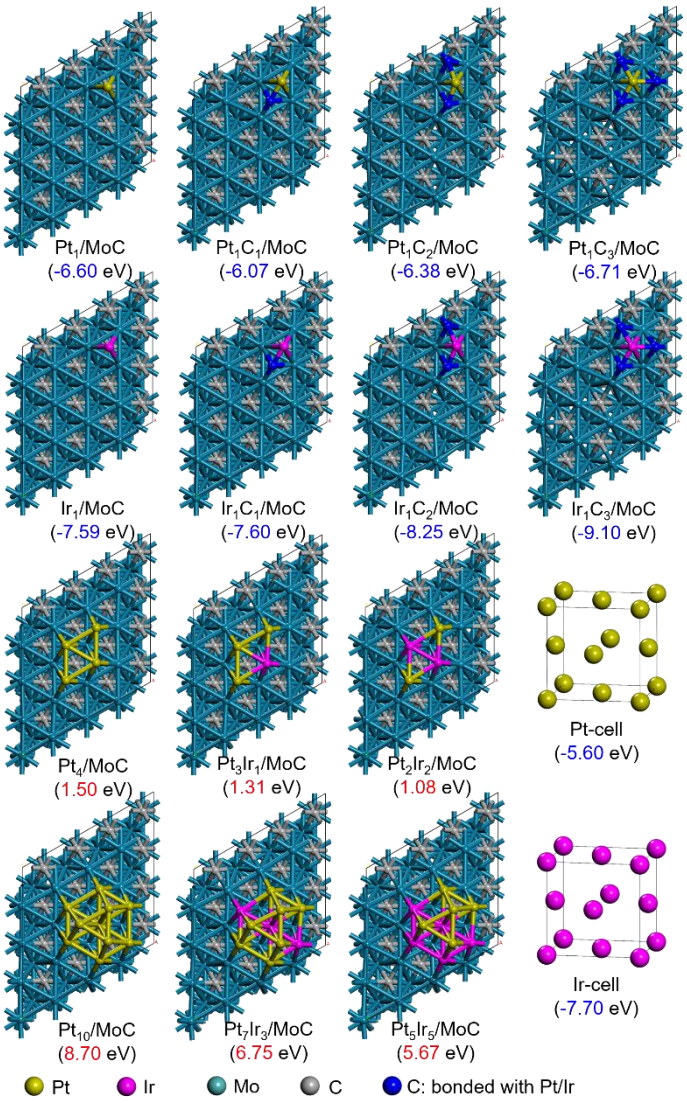

Fig. S31.

Preferential formation of single-atoms and clusters on MoC. DFT-simulated structures of single atoms and clusters on MoC. Binding energies of Pt and Ir single atoms with MoC and their cohesive energies with MoC carbon atoms are shown in blue brackets. Energy differences (ΔE) between clusters and their constituent single atoms are shown in red brackets.

Note:

Firstly, we analyzed the metal-support and metal-metal interactions, specifically focusing on M-MoC and M-M bonding (M= Pt or Ir). The calculations indicate that the binding energy of Pt_1 and Ir_1 on the MoC support is much higher than that in their corresponding Pt or Ir crystal phase, suggesting that both Pt and Ir atoms tend to spontaneously disperse over the MoC support, which is further supported by the *ab initio* molecular dynamic (AIMD) simulations of a Pt_8 cluster on α-MoC(111) , which shows that Pt cluster tends to disperse into highly dispersed atomical Pt species over MoC (see Movies S3-4). Of the M_1/MoC structures, Pt atoms are bonded with MoC through

Pt-Mo bonds while Ir atoms are stabilized by the surface carbon atoms via the formation of Ir_1C_x motifs.

We then calculated the energy differences (ΔE) between the small metal clusters and single metal atoms supported on MoC to evaluate the feasibility of forming specific species. Taking the cluster of Pt_7Ir_3/MoC as an example, the ΔE is calculated by the equation: $\Delta E = E(Pt_7Ir_3/MoC) + 9E(MoC) - 7E(Pt_1/MoC) - 3E(Ir_1/MoC)$, where the $E(Pt_7Ir_3/MoC)$, $E(Pt_1/MoC)$, $E(Ir_1/MoC)$ and $E(MoC)$ are the total energy of Pt_7Ir_3/MoC, Pt_1/MoC, Ir_1/MoC and MoC slab obtained from the DFT optimization, respectively. For M_4 and M_{10} clusters, our calculations suggest that the bi-metallic Pt-Ir clusters are energetically more favorable than mono-metallic Pt clusters of the same size. However, the positive ΔE for both bi-metallic Pt-Ir and mono-metallic Pt clusters indicates that clusters are energetically unfavorable compared to single atoms. Therefore bi-metallic clusters formed during catalyst preparation process tend redisperse into Pt_1 and Ir_1 single atoms in the pre-activation process. Although small clusters are observed under TEM, they may arise from the surface heterogeneity and complexity of the MoC particles, which can accommodate and stabilize these clusters. We must point out that, besides Pt_1/MoC and Ir_1/MoC interfaces, these mono-metallic or bi-metallic clusters are also active for the reaction (see below reply to question c).

Additionally, as Ir_1 single atoms are the most stable atomically dispersed species over MoC surface, they can obstruct potential Ostwald ripening of Pt species.

To summarize, based on experimental and theoretical results, we propose a dual role of Ir in this catalyst system: 1) facilitating the dispersion of Pt by occupying part of the MoC surface sites as Ir_1C_x species; 2) forming Ir_1/MoC active sites to catalyze the selective reforming reaction, thereby contributing to the overall hydrogen/acetic acid production.

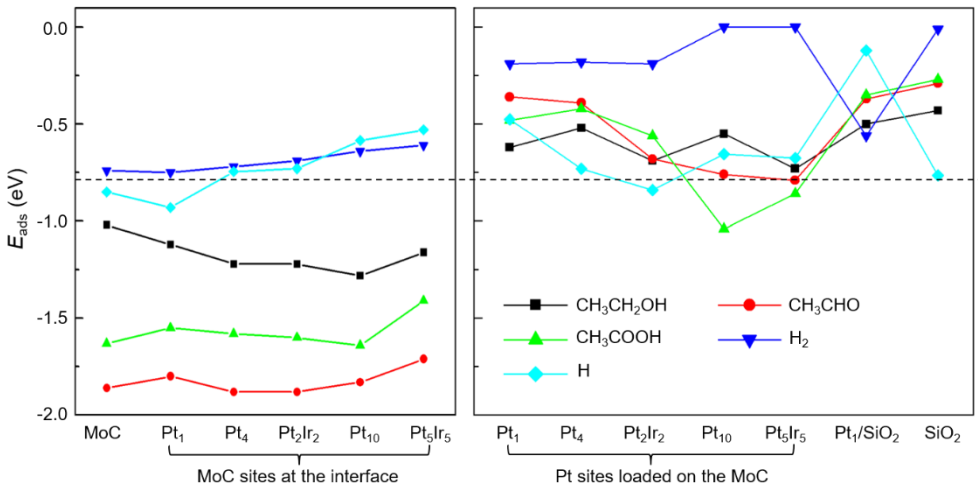

Fig. S32.

Adsorption modulation by Pt/Ir. Adsorption energies of CH_3CH_2OH, CH_3COOH, CH_3CHO, H_2 and H atom on different sites of Pt/Ir based catalysts. Detailed configurations are shown in Figs. S33 to S37

Note:

Our results reveal that the relationship between intermediate adsorption energies on Pt sites versus interfacial MoC sites remains consistent across Pt species with different sizes (Pt_1, Pt_4, Pt_{10}). Key intermediates consistently show stronger adsorption on MoC interface sites compared to metal sites, except for H*. This suggests that the key intermediates are likely to adsorb on MoC interface sites, where the reforming process occurs. Meanwhile, Pt (or Ir) sites primarily serve as sites for H^* adsorption, which significantly modulates the ethanol conversion pathway. These findings align with our calculated results in Fig. 5. This pattern of adsorption behavior persists when shifting from pure Pt to bi-metallic Pt-Ir clusters of the same size. These highly dispersed metal species exhibit structural and adsorption characteristic akin to those of Pt_1/ MoC or Ir_1/MoC sites, contributing to catalytic activity. However, when large particles form on α-MoC surface, C-C bond cleavage happens, leading to the formation of undesired products like CO_2 and CH_4. This highlights the critical role of maintaining highly dispersed metal species to sustain selective reforming activity.

Additionally, we examined the SiO_2 and Pt_1/SiO_2 for comparison. The results show significant difference in adsorption behavior compared to MoC-based models. In particular, the adsorption of substrates and intermediates on Pt_1/SiO_2 is substantially weaker, which limits the progression of the reforming reaction.

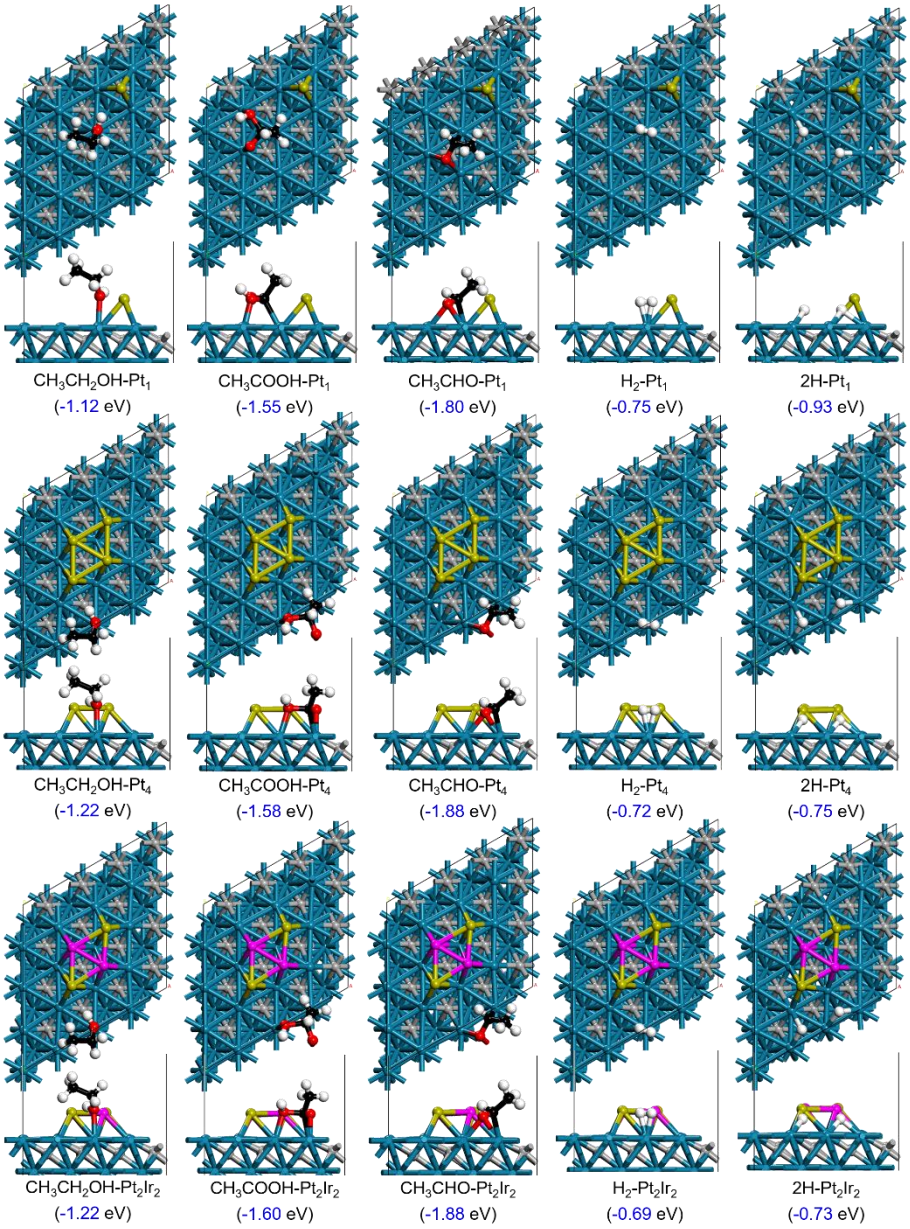

Fig. S33.

Adsorption behavior of substrates/intermediates on interfacial sites of Pt/MoC and Pt_xIr_{4-x}/MoC. Adsorption structures and energies of CH_3CH_2OH, CH_3COOH, CH_3CHO, H_2 and H atom on interface Mo site between MoC and Pt atom/cluster of Pt_1/MoC, Pt_4/MoC, and Pt_2Ir_2/MoC catalysts. Color code: Pt (gold), Ir (pink), Mo (dark cyan), C (grey), O (red), H (white), C from ethanol (black).

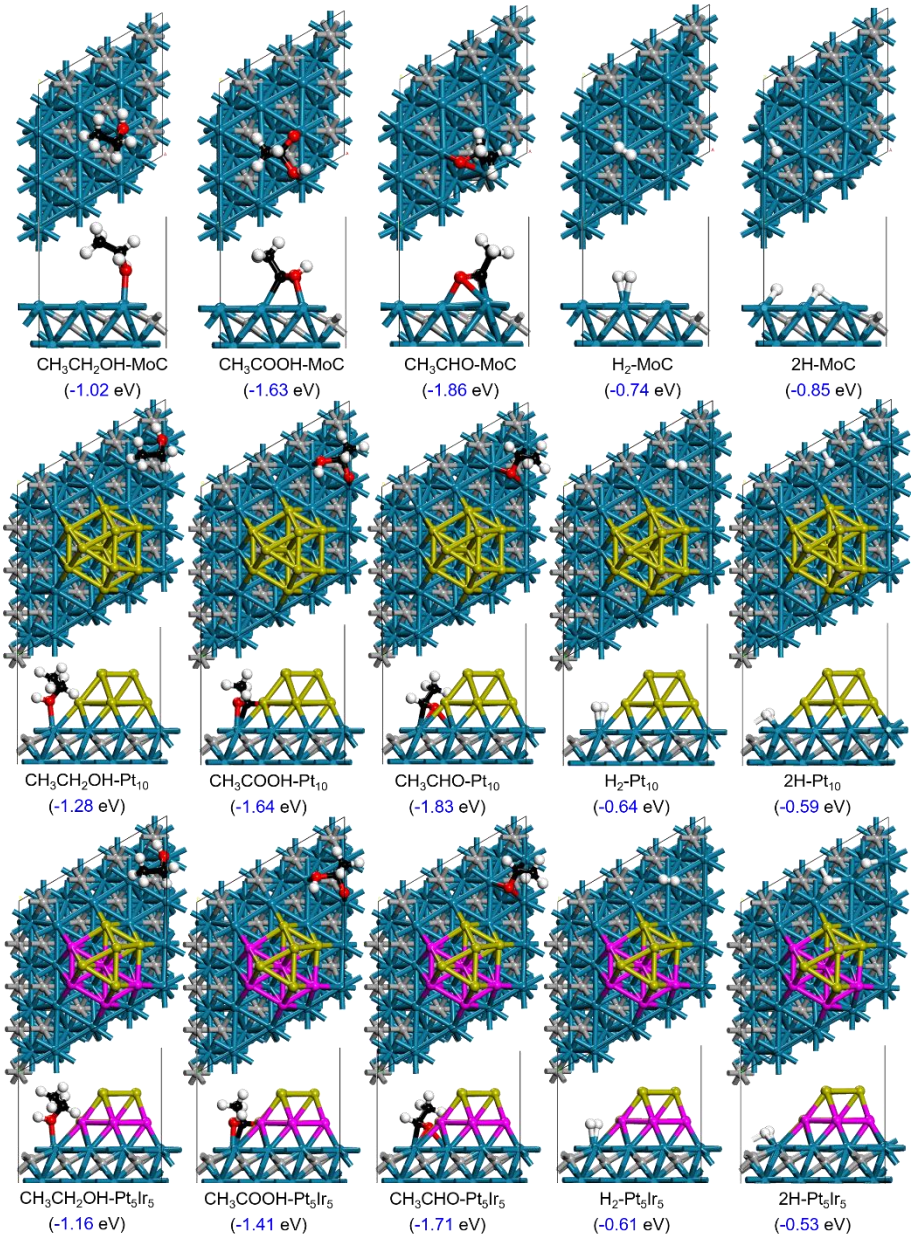

Fig. S34.

Adsorption behavior of substrates/intermediates on interfacial sites of Pt_xIr_{10-x}/MoC. Adsorption structures and energies of CH_3CH_2OH, CH_3COOH, CH_3CHO, H_2 and H atom on the interface Mo site in the catalysts of MoC, Pt_{10}/MoC, and Pt_5Ir_5/MoC. Color code: Pt (gold), Ir (pink), Mo (dark cyan), C (grey), O (red), H (white), C from ethanol (black).

.

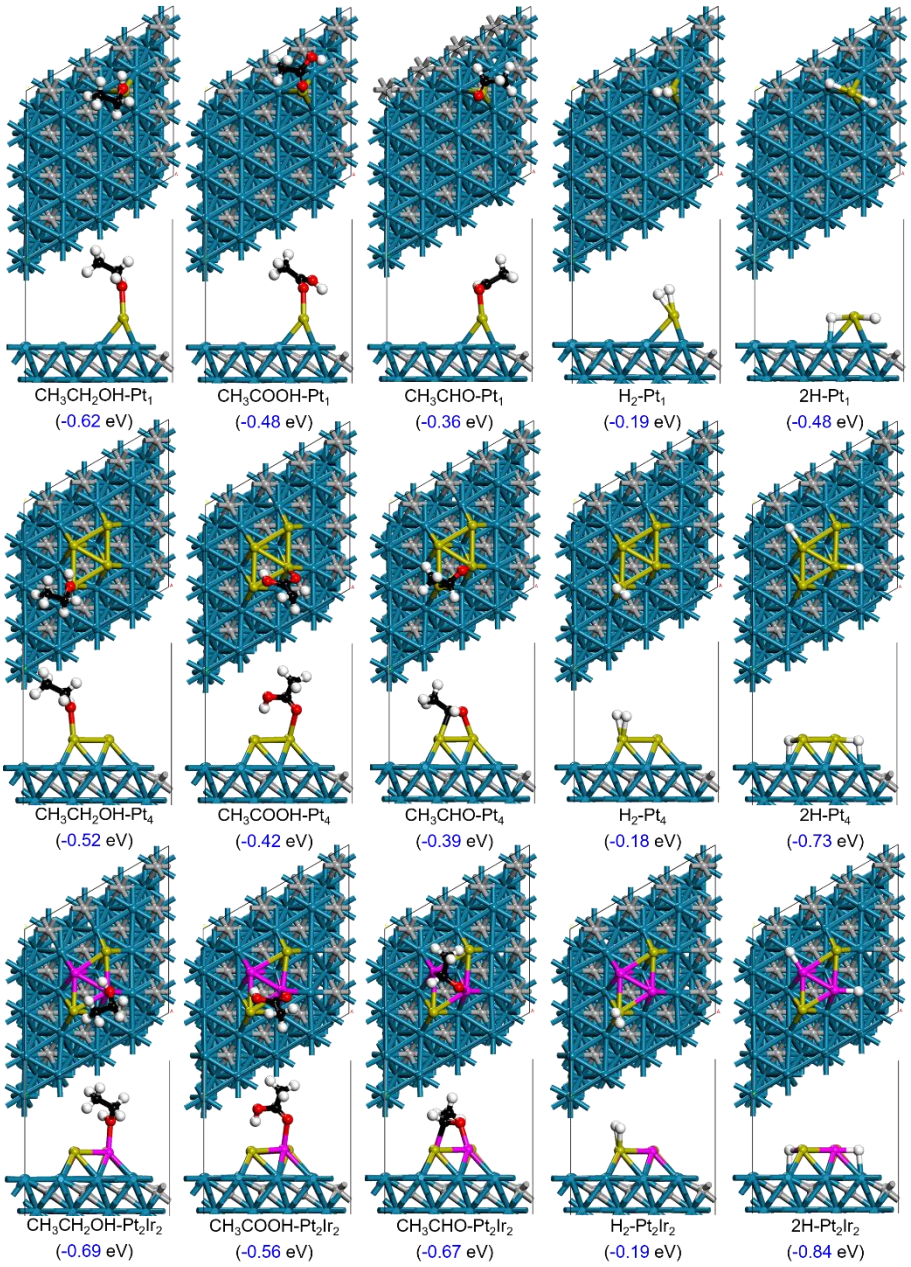

Fig. S35.

Adsorption behavior of substrates/intermediates on Pt sites of Pt/MoC and Pt_xIr_{4-x}/MoC. Adsorption structures and energies of CH_3CH_2OH, CH_3COOH, CH_3CHO, H_2 and H atom on the Pt atom/cluster site in the catalysts of Pt_1/MoC, Pt_4/MoC, and Pt_2Ir_2/MoC. Color code: Pt (gold), Ir (pink), Mo (dark cyan), C (grey), O (red), H (white), C from ethanol (black).

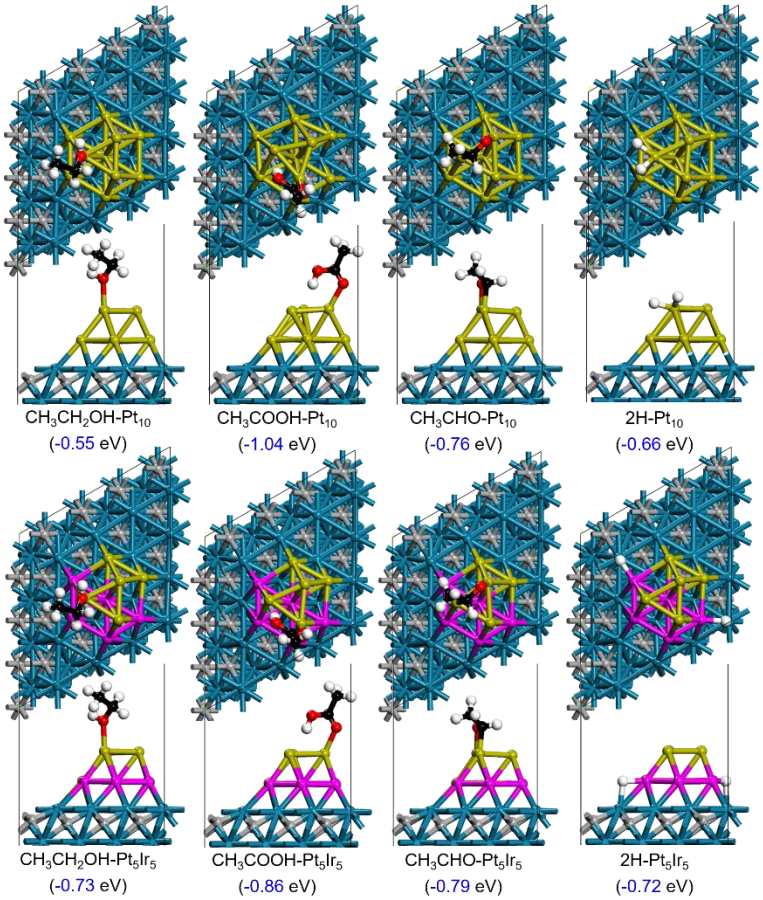

Fig. S36.

Adsorption behavior of substrates/intermediates on Pt sites of Pt_xIr_{10-x}/MoC. Adsorption structures and energies of CH_3CH_2OH, CH_3COOH, CH_3CHO, H_2 and H atom on the Pt cluster site in the catalysts of Pt_{10}/MoC and Pt_5Ir_5/MoC. Color code: Pt (gold), Ir (pink), Mo (dark cyan), C (grey), O (red), H (white), C from ethanol (black).

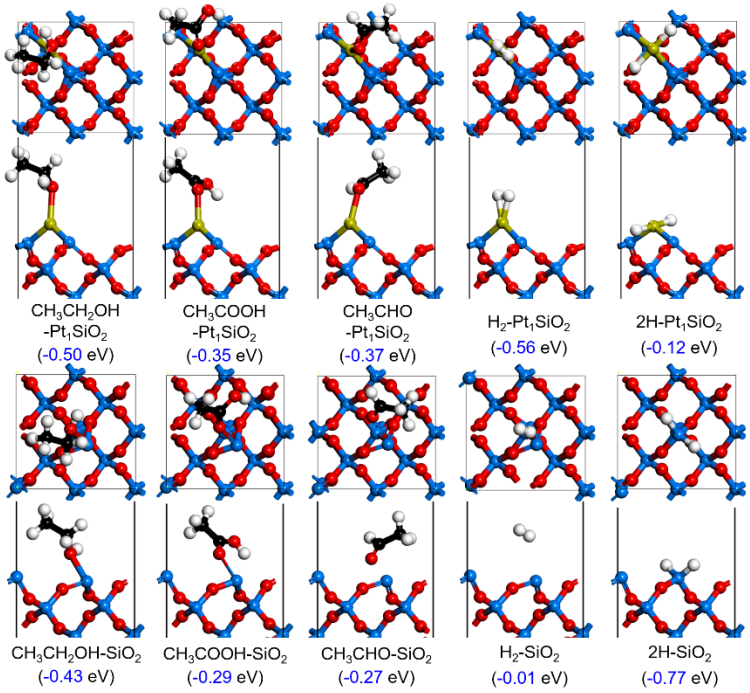

Fig. S37.

Adsorption behavior of substrates/intermediates on Pt sites of Pt_1/SiO_2. Adsorption structures and energies of CH_3CH_2OH, CH_3COOH, CH_3CHO, H_2 and H atom on the Pt site of Pt_1/SiO_2 and SiO_2. Color code: Pt (gold), Si (blue), C (black), O (red), H (white).

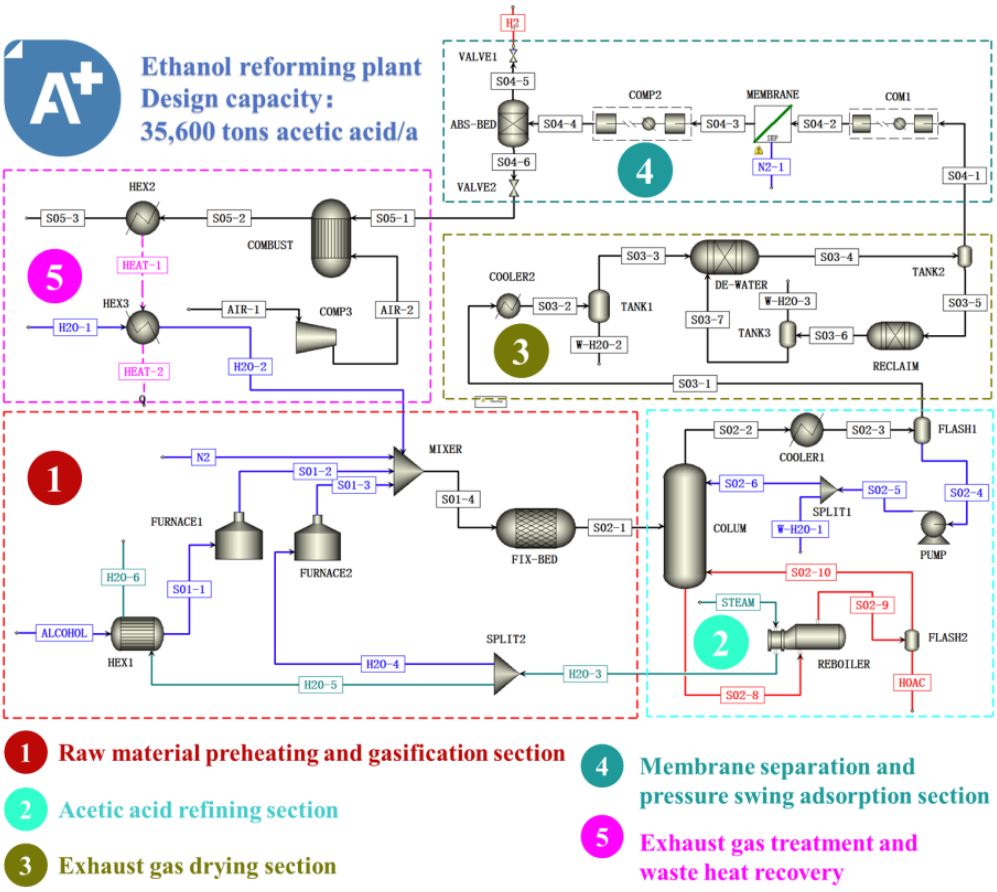

Fig. S38.

Simulated ethanol reforming plant process flow chart.

Note:

The techno-economic analysis and life cycle assessment of this project relies on the preliminary results of laboratory and chemical engineering simulation. The simulation was carried out on process simulation software (Aspen Plus V11). The designed production scale of ethanol reforming is handling 32,400 tons of ethanol per year, which means it produces 36,800 tons of acetic acid and co-produce 26.08 million Nm^3 of hydrogen per year.

The simulated ethanol reforming plant is divided into five sections: 1) Raw material preheating and gasification section; 2) Acetic acid refining section; 3) Exhaust gas drying section; 4) Membrane separation and pressure swing adsorption section; 5) Exhaust gas treatment and waste heat recovery.

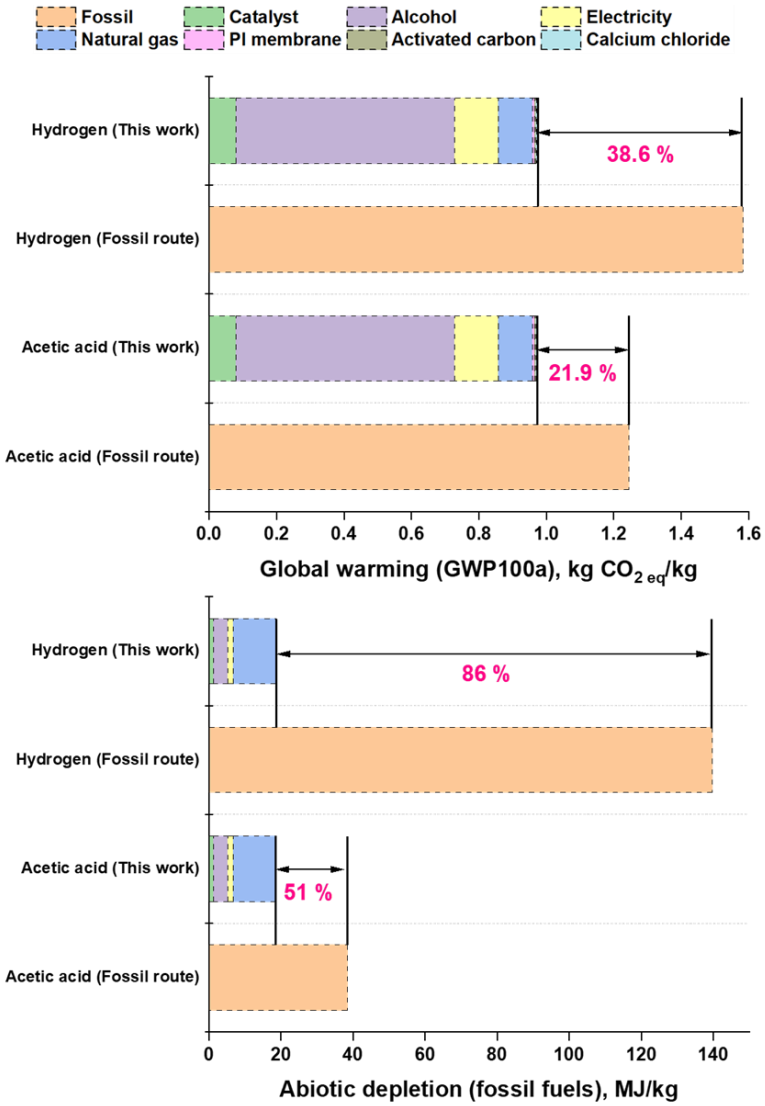

Fig. S39.

Carbon footprint of ethanol selective reforming. Life cycle assessment (LCA) of the ethanol reforming and the contribution rate analysis results.

Note:

The production of acetic acid products achieved a carbon emission reduction of 21.9 %, while hydrogen production achieved a carbon emission reduction of 38.6 %. Notably, the reduction in fossil energy consumption is even more substantial, reaching levels of 51 % to 86 %. In summary, this ethanol reforming plant with a capacity of 36,800 tons of acetic acid can reduce carbon dioxide emissions by approximately 11,505 tons per year. Taking carbon taxes into account, this technology can achieve greater profits by reducing carbon emissions. Based on a carbon emission ratio of \$6.94/ton CO_2, this factory can generate an additional income of \$79,844 by leveraging carbon emissions.

Table S1.
Comparison of energy efficiency and costs of various hydrogen production route.

Entry	Hydrogen production route	Cost ($/kg H_2)	Energy efficiency (%)	Reference
1	SER (ethanol steam reforming)	1.58	80	Ref.(*23*)
2	SMR (steam methane reforming)	2.9	80	Ref.(*24*)
3	Gasification	1.91	35	
4	Pyrolysis	1.6	42.5	
5	Electrolysis	10.3	70	
6	Bio-hydrogen	2.83	0.1	
7	Photocatalysis	9	0.06	
8	Thermochemical cycles	2.31	52	
9	Plasmolysis	6.36	79.2	
10	SSER (selective ethanol steam reforming co-producing acetic acid)	0.20	80	This work

Table S2.

Pt L_3-edge EXAFS fitting results[a] for α-MoC supported PtIr catalyst.

Sample	Shell	C.N.[b]	R(Å)[c]	ΔE_0(eV)	σ^2 (10^{-3} Å^2) [d]	R-factor
Pt foil	Pt-Pt	12.0±0.8	2.763±0.002	7.03	4.56	0.003
1Pt-MoC	Pt-Mo	2.5±0.6	2.74±0.02	0.33	8.38	0.05
	Pt-Pt	1.0±0.3	2.72±0.08		1.31	
3Pt-MoC	Pt-Mo	1.5±0.2	2.71±0.08	2.17	2.78	0.05
	Pt-Pt	3.8±0.3	2.73±0.06		3.38	
6Pt-MoC	Pt-Mo	1.7±0.4	2.73±0.06	4.67	2.31	0.03
	Pt-Pt	4.9±1.7	2.74±0.04		3.48	
3Pt3Ir-MoC	Pt-Mo	4.1±0.7	2.78±0.01	5.79	14.87	0.03
	Pt-O/C	1.1±0.5	1.87±0.03		5.03	
	Pt-Pt(Ir)	2.3±0.3	2.76±0.02		4.46	

a: The data ranges used in the fit are $3.0 \leqslant k \leqslant 10.0$ Å^{-1} (depend on the quality of data) and $1.2 \leqslant R \leqslant 3.0$ Å. *b*: Average coordination number. *c*: The coordination distance. *d*: Debye-Waller factor.

Table S3.

Ir L_3-edge EXAFS fitting results[a] for α-MoC supported Pt/Ir catalysts.

Sample	Shell	C.N.[b]	R(Å)[c]	ΔE_0(eV)	σ^2 (10^{-3} Å^2) [d]	R-factor
Ir foil	Ir-Ir	12.0±1.2	2.707±0.003	9.00	2.82	0.01
1Ir-MoC	Ir-C	1.5±0.3	1.94±0.01	6.84	7.62	0.01
	Ir-Mo	7.6±0.7	2.83±0.03		17.00	
3Ir-MoC	Ir-C	0.9±0.3	1.99±0.08	8.05	0.72	0.01
	Ir-Mo	6.8±1.7	2.89±0.08		13.51	
6Ir-MoC	Ir-C	1.1±0.2	1.99±0.02	10.15	7.69	0.006
	Ir-Mo	1.6±0.7	2.85±0.02		2.53	
	Ir-Ir	1.9±0.5	2.83±0.04		2.08	
3Pt3Ir-MoC	Ir-C	3.2±1.0	1.99±0.03	9.08	2.61	0.02
	Ir-Mo	3.9±0.3	2.85±0.04		9.96	

a: The data ranges used in the fit are $3.0 \leqslant k \leqslant 10.0$ Å^{-1} (depend on the quality of data) and $1.2 \leqslant R \leqslant 3.0$ Å. *b*: Average coordination number. *c*: The coordination distance. *d*: Debye-Waller factor.

Table S4.

The catalytic performance of Pt/Ir based catalysts for selective reforming of ethanol with water

Catalyst	Conversion[a] (%)	Selectivity (%)[b]									Activity ($mmol_{H2}/g_{cat}$ * h)	Carbon Balance[c]
		Acetic Acid	Acetal	Ethyl Acetate	Acetaldehyde	Ethylene	Ethane	Methane	Carbon Monoxide	Carbon Dioxide		
α-MoC	12.5	21.6	1.25	3.12	53	11.4	8.4	0.95	0.320	--	51.3	--
3Pt/α-MoC	40.2	52.1	0.146	1.51	27.6	4.66	3.45	9.28	0.320	0.945	147.3	1.01
3Ir/α-MoC	40.3	58.4	0.142	2.31	27.6	5.83	3.59	1.75	0.309	0.051	176.0	1.09
3Pt3Ir/α-MoC	98.9	84.5	0.100	0.42	3.65	0.747	1.46	4.34	1.31	3.60	331.3	1.05
6Pt/α-MoC	36.6	44.6	0.254	2.24	27.7	2.54	2.97	15.5	0.335	3.88	153.0	1.07
6Ir/α-MoC	31.4	58.5	0.210	1.71	29.5	4.68	3.28	2.02	0.130	--	182.8	1.04
3Pt3Ir/SiO_2	22.6	23.0	0.030	0.100	5.64	0.190	0.600	35.1	31.9	3.12	57.4	--

a. The conversion of ethanol was calculated with the following equation: (total amount of ethanol fed in the reactor - the unreacted ethanol) / total amount of ethanol fed in the reactor.
b. The selectivity of products was calculated based on the number of carbon atoms.
c. The carbon balance was calculated based on the total amount of carbon in and out of the reactor.
d. Reaction conditions: 543 K, $WHSV_{ethanol}$ = 10.6 $g_{ethanol}/(g_{cat} \cdot h)$, carrier gas (5% Ar in N_2) = 60 mL/min, n (ethanol) : n (H_2O) = 1 : 9.

Table S5.

Comparison of hydrogen production through ethanol dehydrogenation/reforming activity in photocatalysis

Entry	Catalyst	H_2 production (mmol/g/h)	Note	Reference
1	PtIr/MoC	331.3	Thermocatalysis	This work
2	Pd/CdS	35.1	Photocatalysis, to 1,1-diethoxyethane	Ref.(*25*)
3	Ni-MoS_2	6.6	Photocatalysis, to 1,1-diethoxyethane	Ref.(*26*)
4	Au/ZnO	0.427	Photocatalysis, to acetaldehyde and acetic acid	Ref.(*27*)
5	$CoTiO_3/TiO_2$	3.7	Photocatalysis, to acetaldehyde	Ref.(*28*)
6	Au@TiO_2	7.09	Photocatalysis, to acetaldehyde	Ref.(*29*)
7	Au/TiO_2	30	Photocatalysis, to acetaldehyde	Ref.(*30*)
8	Pt-Ag/Ag_2PO_4-WO_3	4.01	Photocatalysis, to acetaldehyde	Ref.(*31*)
9	NiCu	176.6	Photo-thermocatalysis (light intensity 574 mW cm^{-2}, temperature 210 °C), to acetaldehyde	Ref.(*32*)
10	gCNT-TiO_2	24	Photocatalysis (light intensity 450 mW cm^{-2}), to acetaldehyde and acetic acid	Ref.(*33*)

Table S6.

Comparison of hydrogen production through ethanol dehydrogenation/reforming activity in electrocatalysis

Entry	Catalyst	Performance	Note	Reference
1	Co-S-P	HER: 167 mV/10 mA cm^{-2}	1M KOH, to acetic acid	Ref.(*34*)
2	3D PdCu alloy	HER: 106 mV/10 mA cm^{-2}	1M KOH, to acetic acid	Ref.(*35*)
3	Pd TNTA	Overall: 0.6 V at 1 mA cm^{-2}	2M KOH, to ethyl acetate	Ref.(*36*)
4	AuPdC	AOR vs RHE: 0.35 V	2M KOH, to ethyl acetate	Ref.(*37*)
5	Ni-Co-polyisocyanurate	-	0.1M KOH, to acetate	Ref.(*38*)
6	Co_3O_4	Overall: 1.5 V at 22 mA cm^{-2}	1M KOH, to ethyl acetate	Ref.(*39*)

Note:

It is difficult to directly compare reforming activity in thermocatalysis with those in electrocatalysis, as the latter is usually normalized on electrochemical surface area (ECSA), besides, the choice of potential in electrocatalysis also significantly impacts the overall activity.

However, most works in electrocatalytic ethanol reforming requires massive concentration of base (such as KOH) to consume the extra protons generated during the reaction, which would be a major drawback for implementation at larger scale.

Table S7.

Comparison of hydrogen generation activity from ethanol reforming at similar reaction conditions (see Figure 4D)

Entryy	Catalyst	Temperature (K)	H_2 production (mmol/g/h)	Reference
1	Pt/CeO_2	523	29.5	Ref.(*40*)
	Pt/CeO_2	573	53.1	
2	$PtNi/CeO_2$	501	80.3	Ref.(*41*)
	$PtNi/CeO_2$	559	160.7	
3	Pd/C	603	22.3	Ref.(*42*)
4	CoO-Pd/Zeolite Y	623	92.8	Ref.(*43*)
5	$Pd\text{-}Ru/Nb_2O_5\text{-}TiO_2$	573	18.5	Ref.(*44*)
6	Pt/CeO_2	473	20	Ref.(*45*)
	Pt/CeO_2	573	130	
7	$LaNiO_3$	473	2	Ref.(*46*)
	$LaNiO_3$	548	56.6	
	$LaNiO_3$	573	97.4	
8	Ni/Y_2O_3	593	25.1	Ref.(*47*)
9	Ni/Cs-Y zeolite	573	24	Ref.(*48*)
10	Ni/ZnO	573	0.94	Ref.(*49*)
	Ni/ZnO	623	2.6	
	10Co1Ni(Na)-ZnO	523	0.0018	
	10Co1Ni(Na)-ZnO	573	4	

Table S8.

Basic investment assumptions

Category		Remark
Total investment	Self-raised funds ratio	55 %
	Bank loan ratio	45 %
Loans	Interest on bank loans	8 % of bank loan
	Loan term	7 years
Fixed asset investment targeted adjustment tax ratio		None
Enterprise income tax		25% of the annual profit
Working capital		Two months of running costs
Annual running time		8000 hr
Reserve fund	Basic reserve funds	15 % of fixed assets
	Reserve fund for price increase	10 % of fixed assets
Industrial land	Industrial land area	10 acres
	Industrial land requisition price	250000 $/acre
Construction	Factory construction period	3 years
Deprecation	Operating life of equipment	15 years
	Residual rate	5 % fixed assets

Note:

Technical and economic analysis will be carried out based on integrated economic analyzer (Aspen Process Economic Analyzer) of AspenTech. This table shows specific operating strategies and investment assumptions of the factory.

Table S9.

Factory equipment and installation costs

Equipment	Equipment cost/$	Installation factor	Installation cost/$	Total/$
HEX1	19400	0.3	5820	25220
FURNACE1	131600	0.3	39480	171080
FURNACE2	193900	0.3	58170	252070
FIX-BED	161600	0.2	32320	193920
COLUM	1037600	0.4	415040	1452640
COOLER1	57900	0.3	17370	75270
FLASH1	24100	0.4	9640	33740
PUMP	5300	0.1	530	5830
REBOILER	49400	0.3	14820	64220
FLASH2	29700	0.4	11880	41580
COOLER2	67500	0.3	20250	87750
TANK1	19100	0.4	7640	26740
DE-WATER	29200	0.2	5840	35040
TANK2	16900	0.4	6760	23660
COM1	1521600	0.2	304320	1825920
MEMBRANE	79300	0.2	15860	95160
COMP2	1033000	0.2	206600	1239600
COMBUST	131600	0.4	52640	184240
COMP3	727300	0.2	145460	872760
	Utility thermal oil system			500000
	Utility steam system			350000
	Recirculating cooling water system			150000
	Total of equipment and installation cost			**7706440**
	Pipeline construction (40% of the equipment cost)			**2134400**
	Instrument electronic control (20% of the equipment cost)			**1067200**
	Subtotal			**10908040**

Table S10.
Other fixed asset expenses

Item	Cost/$
Warehouse	500000
Industrial land acquisition	2500000
Survey and design expense	150000
Technology transfer fee	100000
Engineering insurance rate	150000
Boiler and pressure volume inspection fee	80000
Subtotal of other fixed asset expenses	**3480000**

Note:
Fixed assets include major production equipment, installation and supporting industrial land acquisition and other expenses. The equipment is initially selected, finalized and evaluated through Aspen Process Economic Analyzer. **Table S9** lists the cost and installation engineering costs of major equipment. This part of the cost is nearly 11 million US dollars. **Table S10** shows other fixed capital investment projects, including land, design fees, etc.

Table S11.
Other fixed asset expenses

Project		**Cost/$**	**Remark**
Fixed assets		14388040	Sum of table 3 and 4
Reserve fund	Basic reserve funds	2158206	15 % of fixed assets
	Reserve fund for price increase	1438804	10 % of fixed assets
Working capital		3511034	Two months of running costs
Fixed asset investment targeted adjustment tax ratio		0	Low-carbon policies support enterprise
Interest on bank loans		5180000	The bank loan line is $9.25 million
Subtotal		**26676084**	-

Note:
Based on the fixed asset results in **Table S9-10** and the investment assumptions in **Table S8**, the final total capital investment (TCI) is calculated, and the results are shown in this table.

Table S12.

Operation cost and annual profit of ethanol reforming plant

Raw material	**Unit price ($/kg)**	**Annual consumption (tonne)**	**Cost/$**
Virgin alcohol (53 degrees)	0.2	68800	13760000
Deionized water	0.0028	43375	121450
Calcium chloride	0.21	40	8400
Nitrogen	0.05 $/$Nm^3$	569957 Nm^3	28498
Activated carbon	1.67	3	5010
Molecular sieve	1.11	3	3330
PI membrane	208 $/$m^2$	300 m^2	62400
Subtotal of raw material			**13989088**
Energy and Utilities	Unit price ($/kg)	Annual consumption (tonne)	Cost/$
Electricity	0.14 $/kwh	11859271 kwh	1660298
Natural gas	0.18 $/$Nm^3$	11128000 Nm^3	2003040
Circulating cooling water	0.00007	9090049	636303
Subtotal of energy and utilities			**4299641**
Fixed expenditure			
Direct manufacturing overhead	Labor (70 persons)		972222
	Manual Supervision (15% labor)		145833
	Maintenance (2% of fixed assets)		287761
	Operating supplies (10% of maintenance)		28776
Indirect manufacturing overhead	Property tax (2% of fixed assets)		287761
	Insurance (1% of fixed assets)		143881
	Equipment depreciation		911242
Subtotal of fixed expenditure			**2777476**
Total factory operating costs			**21066205**
Sales return			
Product	Selling price ($/kg)	Yield (tonne)	Total/$
Acetic acid	0.56	36800	20608000
Hydrogen	0.14 $/$Nm^3$	26080000 Nm^3	3651200
Total sales return			**24259200**
Annual profit (pre-tax)			**3192995**
Return on sales (%)			**13.2**

Note:

Besides fixed asset investment, the routine operation of the factory necessitates funds for raw materials, energy, labor, and other expenses. The consumption of energy, raw materials, and auxiliary materials is determined based on Aspen Plus simulation, while the prices of raw materials, energy, and products are determined based on average market prices. This table is a summary of factory operating expenses and sales.

It is important to note that global market prices for raw materials and products vary significantly, making the profitability of this process highly sensitive to regional and temporal factors. By tailoring the process to specific markets and further improving the efficiency of our catalytic

process, we should expect enhanced feasibility and effectiveness. We also anticipate that this process will be particularly favorable for on-site applications where hydrogen production can be integrated with other manufacturing processes, and this diversification can help mitigate the impact of price volatility and increase overall profit margins.

Table S13.

Goal and scope definition of the LCA study

Goal	
Reason for conducting the study	1. This LCA study is used to evaluate the environmental footprint of the ethanol reforming simulation plant; 2. Examine the environmental footprint of acetic acid and hydrogen products from ethanol reforming plant and compare with their traditional production routes; 3. Conduct contribution analysis to find key environmental hot spots.
Audience	Industrial stakeholders, the research community, and the public
Application	Provide technical and theoretical support for carbon emission reduction policies and circular economy
The intention of using results in a comparative study	Yes, the results are to be compared and disclosed to the public through this article publication.
Scope	
System boundary	Gate-to-gate
Functional unit	1 kg of acetic acid or hydrogen
Allocation	Mass allocation
Assumptions	(I) This factory deals with approximately 8600 kg alcohol (53 degrees) per hour over 8,000 hours per year. (II) This factory produces approximately 4600 kg acetic acid and 300 kg hydrogen per hour over 8,000 hours per year.
Requirements on data and quality	Foreground material and energy consumption data were obtained from laboratory results and Aspen Plus simulation. The background processes were chosen based on Ecoinvent V.3.8 in Open LCA v1.11.0 to cover the technological and geographical representativeness.
LCIA methodology	CML-IA baseline
Impact categories	(II) Abiotic depletion (fossil fuels), MJ; (VI) Global warming (GWP100a), kg $CO_{2\ eq}$;
Limitations	In addition to the above-mentioned assumptions, the following aspects are not assessed in this study: Plant construction and equipment maintenance.
Report requirements	To present the outcome via journal publication which is openly accessible to everyone.

Note:

An environmental impact assessment of the entire simulated plant was conducted using the life cycle assessment (LCA) approach. While LCA can evaluate various environmental footprints, this project focuses on tracking two widely concerning environmental indicators: carbon footprint and non-renewable energy consumption, for simplicity. The detailed LCA objectives, survey scope, functional units, and other settings are listed in this table. The system boundary of LCA is "Gate-to-gate", that is, from the time alcohol enters the factory until the products (acetic

acid and hydrogen) leave the factory, the transportation of raw materials is not taken into account.

Movie S1.
Experimental 3D atomic model of 3Pt/α-MoC

Movie S2.
Experimental 3D atomic model of 3Pt3Ir/α-MoC

Movie S3.
The AIMD simulation of Pt_8 on α-MoC (top view)

Movie S4.
The AIMD simulation of Pt_8 on α-MoC (side view)